Acta Pharmaceutica Sinica B 2025;15(4):2077−2094

Chinese Pharmaceutical Association
Institute of Materia Medica, Chinese Academy of Medical Sciences

Acta Pharmaceutica Sinica B

www.elsevier.com/locate/apsb
www.sciencedirect.com

ORIGINAL ARTICLE

Acteoside ameliorates hepatocyte ferroptosis and hepatic ischemia-reperfusion injury *via* targeting PCBP2

Kexin Jia[a], Yinhao Zhang[a], Fanghong Li[b], Runping Liu[b], Jianzhi Wu[a], Jiaorong Qu[a], Ranyi Luo[a], Zixi Huang[a], Zhe Xu[a], Xiaojiaoyang Li[a,*]

[a]*School of Life Sciences, Beijing University of Chinese Medicine, Beijing 100029, China*
[b]*School of Chinese Materia Medica, Beijing University of Chinese Medicine, Beijing 100029, China*

Received 23 June 2024; received in revised form 10 December 2024; accepted 20 December 2024

KEY WORDS

Acteoside;
Hepatic ischemia−reperfusion injury;
Ferroptosis;
PCBP2;
System Xc^-;
HMGB1;
Macrophage polarization

Abstract Hepatic ischemia-reperfusion injury (HIRI) has been considered as an inevitable process of liver transplantation. Hepatocyte ferroptosis is a key factor in HIRI development, yet precise mechanism and potential therapies are still unclear. Here, we demonstrated a strong correlation between hepatocyte ferroptosis and the downregulation of poly(rC)-binding protein (PCBP2), which compromised the stability of antiporter system Xc^- (consisted of SL3A2/SLC7A11). Besides, inhibiting PCBP2 contributed to facilitating cofactor p300 to enhance the transcriptional activity of HIF1α, leading to the expression and secretion of HMGB1. Then, released HMGB1 from ferroptotic hepatocytes worsened M1 macrophage recruitment and immune response during HIRI. Additionally, acteoside (ACT) was shown to assist PCBP2 in stabilizing the mRNA stability of *Slc3a2* and *Slc7a11*, as well as enhance the binding affinity of PCBP2−system Xc^-. Beyond that, ACT also supported PCBP2 to limit HMGB1-induced M1 macrophage recruitment through imposing restrictions on p300 and HIF1α. Furthermore, specific knockdown of PCBP2 in hepatocytes directly interposed the therapeutic efficacy of ACT on HIRI mice. In conclusion, ACT alleviated hepatocyte ferroptosis and HIRI *via* promoting PCBP2 to maintain the stability of system Xc^- and limit HIF1α/p300−HMGB1 signaling. These findings highlight the therapeutic benefits of ACT in treating HIRI and offer insights into innovative therapeutic strategies.

*Corresponding author.
E-mail address: xiaojiaoyang.li@bucm.edu.cn (Xiaojiaoyang Li).

Peer review under the responsibility of Chinese Pharmaceutical Association and Institute of Materia Medica, Chinese Academy of Medical Sciences.

https://doi.org/10.1016/j.apsb.2025.03.002

1. Introduction

Hepatic ischemia−reperfusion injury (HIRI) is a two-interrelated complex complication that arises in scenarios such as hemorrhagic shock, hepatectomy, and liver transplantation. This condition inevitably leads to hepatocellular damage, thereby increasing the risk of hepatic dysfunction, liver fibrosis, and even liver failure[1,2]. Importantly, hepatocyte damage begins during the ischemia stage and continues throughout HIRI, primarily caused by oxidative stress and the ensuing inflammatory response due to inadequate blood oxygenation[3,4]. As our understanding of the etiology and pathogenesis of HIRI deepens, research has found that inhibition of excessive oxidative stress and abnormal cell death caused by different reasons like ferroptosis or improvement of complex immune responses within the hepatic sinusoidal microenvironment can attenuate liver injury and improve hepatic function under HIRI insult to varying degrees[5]. Until now, the urgent need for more accurate solutions for damaged hepatocytes during and even after HIRI process cannot be overstated. Given the significant clinical implication of HIRI, it is of great significance to uncover the potential mechanisms and establish therapeutic strategies.

Recently, the role of ferroptosis in the HIRI process has received increasing attention, which is characterized by excessive iron accumulation, the buildup of reactive oxygen species (ROS), and swollen mitochondria with the loss of cristae, ultimately resulting in the secretion of damage-associated molecular patterns (DAMPs) and disturbance of other hepatic cells[6]. Once ischemia and hypoxia occur, injured hepatocytes overproduce the iron ion [ferrous ion (Fe^{2+}) and ferric ion (Fe^{3+})], driving the cascaded peroxidation chain reaction, as accompanied with the suppressed antioxidant axis of glutathione (GSH)/glutathione peroxidase 4 (GPX4). Prior studies have reported that the generation of GSH is regulated by the transportation of extracellular L-cystine and intracellular L-glutamic acid through system Xc^-, the cystine (Cys)-glutamate antiporter, which consists of a light chain (called SLC7A11 or xCT) and a heavy chain (called SLC3A2 or CD98hc). Of note, the poly(rC)-binding protein 2 (PCBP2) has been reported to limit the ferroptosis of hepatocytes not only *via* delivering iron ions to ferritin as an iron chaperone but also contributing to the mRNA stabilization of *Slc7a11* as an RNA binding protein (RBP)[7-9]. However, the effects and potential mechanisms of PCBP2 on the stability of system Xc^-, hepatocyte ferroptosis and the resultant HIRI have not yet been investigated.

Numerous natural products serve as crucial sources of inspiration for the discovery and development of targeted drugs. Acteoside (ACT), a variety of phenylpropanoid glycoside, has been demonstrated to effectively alleviate hepatocyte apoptosis, oxidative stress, and local inflammation in various liver diseases[10-12]. Most recently, we first noticed that ACT could inhibit the transfer of hepatocyte-derived DAMPs to liver sinusoidal endothelial cells (LSECs), thereby reversing the aging fate of LSECs and improving the microenvironment of hepatic sinusoid stimulated by surgical ischemia and hypoxia damage[10]. Notably, to date, there is still a lack of research evidence demonstrating that ACT can alleviate HIRI through the direct improvement of ferroptosis, we recently verified that the aqueous extract containing the amount of ACT alleviated ferroptosis and HIRI through improving the SLC39A14-hepcidin mediated cellular iron homeostasis of hepatocytes[13]. Therefore, further substantiation supporting the causal relationship between the regulation of ferroptosis-related PCBP2/system Xc^- signaling and ACT-induced hepatoprotection needs to be provided.

In this study, we employed RNA sequencing (RNA-Seq) to analyze a specific subtype of hepatocytes as well as whole liver samples, in conjunction with other molecular biological experiments, thereby confirming that PCBP2 was a novel suppressor of ferroptosis in hepatocytes during HIRI. Both HIRI *in vivo* and hypoxia and reoxygenation (HR) *in vitro* stimulation suppressed the hepatic PCBP2 expression, leading to a loss of its ability to stabilize system Xc^- and promote high mobility group box-1 protein (HMGB1) secretion by enhancing the transcriptional activity of HIF1α and its co-activator E1A binding protein p300 (p300), and ultimately the macrophage recruitment and inflammation activation. Interestingly, ACT decreased the susceptibility of ferroptosis in hepatocytes and reversed HIRI by repairing above PCBP2-mediated signaling, which was partially blocked by siRNA targeting PBCP2 *in vitro* or the injection of PCBP2-silencing hepatocyte-targeting lipoplexes *in vivo*. This study not only presents a novel perspective on the role of PCBP2/system Xc^- axis in HIRI and other ferroptosis-related diseases, but also lays the groundwork for perfecting the potential therapeutic strategies to prevent HIRI.

2. Materials and methods

2.1. Materials

ACT (S31661), cholera toxin B (CTB, S89373), erastin (S80804), ferrostatin-1 (fer-1, S81461), and gadolinium trichloride ($GdCl_3$, S40195-259) were used in this study (Yuanye biotechnology, Shanghai, China). The recombinant HMGB1 (HY-P73104) and actinomycin D (AD, HY-17559) were employed (MedChemExpress, NJ, USA). The recombinant PCBP2 protein (CSB-EP622995HU) was applied both *in vivo* and *in vitro* (CUSABIO, Wuhan, China). Cell culture consumable reagents were applied *in vitro* experiment (Sigma−Aldrich, St. Louis, MO, USA). The information regarding the utilized antibodies was documented in Supporting Information Table S1.

2.2. Animal studies

C57BL/6J mice (male, 8-week-old, 24−26 g) were housed in the humane-care environment under a 12 h light/dark cycle with suitable germ-free feeding for 1-week adaptation (SiPeiFu biotechnology, Beijing, China). All animal experimental procedures were approved by the Ethics Committee of the Institutional Animal Care and Use Committee of Beijing University of Chinese Medicine (Beijing, China). Thirty-six mice were separated into 6 groups randomly: sham group; HIRI group; HIRI plus low,

medium or high doses of ACT groups (25, 50 and 100 mg/kg); HIRI plus *N*-acetyl-L-cysteine (NAC) positive group (100 mg/kg). Mice in sham and HIRI groups were intraperitoneally injected 100 mg/kg of physiological saline as a parallel control. Simultaneously, the mice in ACT groups and NAC group were intraperitoneally injected with relative drugs for 7 days before the operation. Of noted, the reference doses of ACT were based on the reported dosages and our previous study[10,14-16]. For the HIRI model establishment, mice were continuously anesthetized with the gas isoflurane using the Inhalational Anesthesia Systems (RWD Life Science, Shenzhen, China). Then the abdomen of mice was cut transversely below the xiphoid, and cephalad lobes of hepar were occluded by an atraumatic vascular clamp to generate the liver ischemia for 1 h, after that, the non-invasive clip was removed lightly to initiate the following reperfusion of liver tissue. Meanwhile, sham operation mice were only subjected to abdomen exposure and wound suture. After 6 h post-operation, all mice were euthanized to obtain the blood and liver samples for subsequent experiments.

Briefly, for caudal injection of PCBP2-silencing hepatocyte-targeting lipoplexes, the Lipofectamine 2000 (Hanheng biotech, Shanghai, China) at 125 μL was activated by 30 μg polyethylene glycol maleimide (Yuanye biotechnology, Shanghai, China) and the mixture was incubated at 75 °C for 30 min. The purified apolipoprotein E (ApoE) (MedChemExpress, NJ, USA) was then incubated with iminothiolane hydrochloride (2-IT) at a molar ration 1:2 and dissolved in phosphate-buffered saline at 25 °C for 90 min. Subsequently, under the nitrogen atmosphere, the Lipofectamine 2000 (125 μL) was activated and then conjugated to ApoE (1.24 μL) at 25 °C for 4 h. Finally, the mixture of 2-IT and glycine was incubated in phosphate-buffered saline solution at 25 °C for 2 h with a molar ratio of 1:2. After that, the ApoE-Lipofectamine 2000 solution (125 μL) was purified by adding the mixture of glycine and 2-IT (1 μL), and allowing the two components to react at 25 °C for 60 min, which were then incubated with si-negative control (si-NC) or si-PCBP2 (5 μL siRNA per mixture liquids 1000 μL) at 25 °C for 12 h to prepare the ApoE-conjugated lipoplexes nanoparticles (LNPs). Then, mice were randomly allocated into 4 groups ($n = 6$): sham plus si-NC LNPs group; HIRI plus si-NC LNPs group; HIRI plus LNPs-si-PCBP2 group; HIRI plus LNPs-si-PCBP2 plus ACT group (50 mg/kg). The drug administration, surgical procedures, and anesthetic protocols for the animal experiments were consistent with the above batches.

2.3. Cell culture and treatment

AML 12 cells (murine hepatocyte cell line), RAW 264.7 cells (murine macrophages), and THP-1 cells (human leukemia monocytic cell line) were cultured in the 37 °C cell incubator with the 95% O_2−5% CO_2 ventilation (BNBIO biotechnology, Beijing, China). The HR system *in vitro* to mimic the HIRI state in the clinic was established as previously mentioned[10]. Briefly, AML 12 cells were placed into the Microaerophilic Culture Incubator HF100 (Heal Force, Shanghai, China) with the 94% N_2−1% O_2−5% CO_2 aeration for 12 h, then were subjected to reoxygenation by being cultured under standard conditions at 37 °C and 5% CO_2 for an additional 8 h. AML 12 cells were 12 h-pretreted with ACT in different doses (25, 50 and 100 μmol/L) under the HR insult, and treated with fer-1 (ferroptosis inhibitor, 1 μmol/L) for 1 h before cells and culture medium being harvested. Meanwhile, for better matching the ferroptosis circumstance, AML 12 cells were also stimulated by a ferroptosis inducer erastin (10 μmol/L) with the treatment of ACT and fer-1 similar to the above HR system. For Pcbp2 silencing experiment, AML 12 cells were transfected with siRNA (5′-TCCTGAGAGAATTATCACTTT-3′) by Lipofectamine RNAi MAX Transfection Reagent (Hanheng, Shanghai, China) in Opti-MEM medium for 48 h with ACT (25, 50 and 100 μmol/L) and Fer-1 pre-incubated for 1 h. The Opti-MEM medium was subsequently replaced with a medium supplemented with 10% fetal bovine serum (FBS). Upon completion of different treatments, all AML 12 cells and culture medium were collected for further experiments. For the establishment of hepatocyte-macrophage co-culture transwell system, the prepared hepatocytes (control group, HR group, HR + 50 μmol/L ACT group, erastin group and erastin +50 μmol/L ACT group) were seeded in the downward chamber and macrophages were cultured in the upper chamber of 24-well transwell culture plated using 1% fetal bovine serum medium for 24 h. Then the macrophage migration was observed and analyzed by the crystal violet staining, and the quantity of migrated cells was analyzed by the DM68 Fluorescence Microscope (Leica, Wetzlar, Germany).

2.4. RNA-sequencing of mouse livers and primary hepatocytes

For the whole liver-seq, the sequencing library was established by extracting and quantifying total RNA from mouse liver. RNA integrity was assessed using the RNA Nano assay, followed by mRNA purification using poly-T oligo-attached magnetic beads. Subsequently, cDNA fragments in the 250−300 bp range were purified and enriched with AMPure XP after cDNA synthesis. Finally, the NEBNext Ultra RNA Library Prep Kit (NEB) was used to prepare the sequencing library, which was then sequenced on the Illumina Novaseq platform.

For the murine hepatocytes RNA-seq, mice were undergoing surgical modeling and intragastric administration of ACT as described above. At the end of treatment, primary hepatocytes from different groups were isolated and purified using collagenase and percoll methods. Total RNA was extracted from the hepatocytes using the Trizol Kit (Invitrogen, CA, USA), followed by reverse transcription to cDNA using the cDNA Reverse Transcription Kit (Vazyme, Nanjing, China). Subsequently, the sample quantification was performed by the NanoRhatometer Spectrophotometer (IMPLEN, Munich, Germany). Furthermore, the cells-RNA sequencing library was established on the Illumina Novaseq platform following the same procedures as described for total liver samples. The sequencing samples were standardized and differentially expressed genes (DEGs) were analyzed using the edgeR. The Cluster Profiler R package was used for enrichment analysis of DEGs, while the Gene Ontology (https://geneontology.org/), STRING (https://string-db.org/) and KEGG (https://www.kegg.jp/) database were utilized for signaling pathway analysis. The Gene Set Enrichment Analysis (GSEA) was performed by the GSEA software (https://www.gsea-msigdb.org/gsea/index.jsp). The bioinformatics website (https://www.bioinformatics.com.cn/) and Sangerbox database (http://www.sangerbox.com/) generated the gene heatmap, violin plots and circle graph. Benjamini adjusted P value < 0.05 was recommended to report the significant difference.

2.5. Total iron and ferrous iron assay

To determine the level of total iron and ferrous iron in liver tissue, we used the Iron Colorimetric assay Kit (Elabscience Biotech, Wuhan, China). Firstly, the mice livers from different groups were

cut in a certain weight and split in lysis buffer. Then the samples were centrifugated and the supernatants were collected for the following iron concentration detection. The samples (0.1 mL) were individually mixed with the deionized water (0.1 mL) and chromogenic agent (0.4 mL), and then centrifuged at 3000 × *g* for 10 min. Subsequently, the supernatants were collected for measuring the OD at 520 nm. And the contents of Fe^{3+} and Fe^{2+} were analyzed according to the standard curve.

For the evaluation of Fe^{3+} and Fe^{2+} contents *in vitro*, the overnight cultured cells were harvested and subsequently suspended in PBS, and the cells were lysed by ultrasonic crash to release intracellular total iron and ferrous iron. Then the cell supernatants were obtained and mixed with the deionized water, iron standard stock solution and chromogenic agent orderly, which boiled and centrifuged as above-mentioned. After that, the cellular Fe^{3+} and Fe^{2+} contents were tested at 520 nm.

2.6. Surface plasmon resonance (SPR)

To detect the binding affinity of ACT and PCBP2, we performed the SPR measurement by the Biacore SPR Instrument (Cytiva, Uppsala, Sweden). In brief, purified PCBP2 proteins (20 μg/mL, pH 4.5) were attached to the CM5 Sensor Chip (Cytiva, Uppsala, Sweden) on 5400 response units (RU). Phosphate-buffered saline (1 ×) was used as the running buffer for immobilization. Then, the ACT was diluted into the concentrations of 0, 1.25, 10, 25, 50, 75 and 100 μmol/L and successively flowed through the PCBP2 protein (parameter: 30 μL/min, binding time 60 s, dissociation time 60 s). Then final graph was analyzed by fitting the binding curve and was reflected by the equilibrium dissociation constant (K_D).

2.7. Microscale thermophoresis (MST)

The MST assay was performed by the Monolith NT.115 Instrument (NanoTemper Technologies, Munich, Germany). The PCBP2 protein was fluorescently labeled for 30 min in the dark place according to the manufacturer's protocol. The 1 mmol/L ACT was diluted into 16 concentrations in a double-dilution way and respectively incubated with 5 μmol/L of purified labeled PCBP2 protein of an equal volume in running buffer. Then, the well-mixed samples were loaded into glass capillaries and further detected in the NanoTemper Instrument (NanoTemper Technologies, Munich, Germany), with the K_D value being calculated.

2.8. PCBP2−SLC7A11/SLC3A2 interaction and protein binding simulation

To investigate the interactions of PCBP2−SLC3A2 and PCBP2−SLC7A11, we utilized the database RCSB (https://www.rcsb.org/) and ZDOCK (https://zdock.umassmed.edu/) to identify existing and potential associations, as well as simulate the protein−protein complexes. The PyMOL software (https://pymol.org/2/) and Auto-Dock Tools (https://en.freedownloadmanager.org) were utilized for the visualization and modification of proteins and ACT structures, respectively. Docking simulations were conducted using the Molecular Operating Environment docking system (MOE: https://www.chemcomp.com/Products.htm), employing processed protein structures as ligands to analyze docked target proteins. Protein docking complexes were visualized utilizing PyMOL software.

2.9. Multiplex immunohistochemical staining

For the fluorescent multiplex immunohistochemistry assay, a four-fluorescence kit based on tyramide signal amplification (TSA) was used following the manufacturer's protocol (Recordbio, Shanghai, China). Briefly, after the antigen retrieval, the liver tissues were firstly incubated with the primary antibody of PCBP2, following the secondary antibodies (Beyotime, Shanghai, China) and TSA solution for AlexaFluor450. Then the primary antibodies of SLC3A2 and SLC7A11 were in the above protocol in two sequential cycles with TSA solution AlexaFluor488 and AlexaFluor594, respectively. The fluorescent images were captured with the Fluorescence Microscope (Olympus, Tokyo, Japan).

2.10. Flow cytometry analysis

Primary mouse macrophages were extracted and purified as previously described[17]. The cells in sample tubes were resuspended using cell staining buffer and supplemented with a 2 μg CD16/CD32 receptor-blocking agent per well. The mixture was then incubated at room temperature for 20 min. Next, individual additions of CD45, F4/80, CD11b and CD11c were added to the sample tubes which were subsequently incubated in darkness at 4 °C for 30 min. Following these steps, all tubes were subjected to two washes with staining buffer under dark conditions prior to a final wash and resuspension for subsequent analysis.

2.11. Physicochemical characterization of LNPs

For the morphology and size determinations of LNPs, transmission electron microscopy (TEM) was performed. Briefly, the prepared LNPs were quickly frozen and then cooled, and moved to the microscope for imaging (JEM 1200EX, JEOL, Japan). The encapsulation efficiency (EE%) of si-PCBP2 in LNPs was measured by fluorescence spectrum and high-performance liquid chromatography. For the LNPs stability detection, the hydrodynamic diameters, zeta-potential values and polydispersity indexes (PDI) of LNPs were measured by dynamic light scattering (DLS) using a Zetasizer (Malvern Co., Malven, UK). The long-time stability of LNPs was determined both in PBS and cell culture media, with the diameters being measured at different time intervals in 35 days. For the si-PCBP2 release test, the free siRNA and si-PCBP2 loaded LNPs were assessed using dialysis method as previously reported[18]. LNPs were transferred into the dialysis membrane bag and immersed in PBS at room temperature. Subsequently, the concentration of released siRNA was measured by nanodrop in multi-time intervals (6−120 h). The release curve was calculated based on the cumulative released siRNA. For testing the hepatocytes-targeting ability of LNPs-si-PCBP2 *in vivo*, the DIR-labeled si-NC LNPs and DIR-labeled LNPs-si-PCBP2 conjugated with ApoE were prepared and tail-intravenously injected into mice. Then the fluorescence distributions of LNPs *in vivo* were detected by the IVIS Imaging System (PerkinElmer, Massachusetts, USA) at 6 h post-injection. Meanwhile, the other mice administrated by LNPs-si-PCBP2 were sacrificed at 0, 2, 4, 6 h post-injection. Then, the different organs including heart, kidney, spleen and liver were harvested and observed under the living image system for further analysis.

2.12. Statistical analysis

The experimental data were presented as the mean ± standard deviation (SD) and repeated at least three times. Statistical

analyses were conducted using GraphPad Prism version 8.0.2. All statistical details, including $P < 0.05$ significance, are included in the figures and relative figure legends. The supplementary file provides additional information and methodology details.

3. Results

3.1. The protective effect of ACT on HIRI-induced liver damage may be related to the inhibition of ferroptosis

To clarify the hepatoprotective effects and underlying mechanisms of ACT in alleviating HIRI, we performed liver function tests, histological examination and transcriptomic sequencing of mouse livers from all groups with or without ACT treatment. Biochemical assays verified that HIRI markedly induced hepatic injuries and oxidative stress, as indicated by the elevated level of aspartate transaminase (AST) and alanine transaminase (ALT), malondialdehyde (MDA) and decreased superoxide dismutase (SOD), which could be significantly protected by ACT or positive drug NAC administration (Fig. 1A and Supporting Information Fig. S1A). Besides, the large-scale ischemic and inflammatory infiltrated region in the HIRI livers were also ameliorated by ACT as shown in liver images, hematoxylin & eosin (H&E) staining and relevant Suziki score (Fig. 1B and Fig. S1B). To further reveal the underlying mechanism of ACT on HIRI, 20357 genes and 22650 genes have been analyzed by RNA sequencing in HIRI group *vs* Sham group (1296 genes were upregulated and 1229 genes were downregulated) and HIRI + ACT group *vs* HIRI group (146 genes were upregulated and 282 genes were downregulated), respectively (Fig. 1C). Furthermore, the Gene Ontology enrichment analysis demonstrated that, compared to sham-operated mice, a significant proportion of DEGs in HIRI mice were enriched in pathways related to ferroptosis, including the oxidation reduction process, glutathione (GSH) metabolic process, lipid metabolism and iron ion binding (Fig. 1D). Subsequently, we conducted a comparative analysis of the transcriptional changes induced by sham operation, HIRI operation and HIRI with ACT treatment using GSEA. The GSEA enrichment plots unveiled a remarkable down-regulation of ferroptosis-related pathways, encompassing lipid peroxidation and mitochondria-associated pathway, in ACT-treated mice subjected to HIRI injury as compared to those in HIRI mice (Fig. 1E and F). These results suggest that ferroptosis may be a key link in ACT's ability to alleviate HIRI.

3.2. ACT improves hepatocyte ferroptosis and hepatic damage both in vivo and in vitro

To better characterize ferroptosis in hepatocytes of the liver subjected to HIRI, as a well-recognized ferroptotic model *in vivo*[5], we examined liver structure and biochemical markers in mice from different groups. Compared with the sham-operated livers, the immunofluorescence intensity of TUNEL image was heightened in the HIRI group but dramatically decreased in the groups treated with different dosages of ACT (25, 50 and 100 mg/kg) (Fig. 2A and Supporting Information Fig. S2A). More specifically, the hepatocyte apoptosis initiated from mitochondrial damage in HIRI group but not in ACT-treated groups as observed in the TEM images (Fig. 2B), which clearly displayed the characteristic signs of injured mitochondrial structure with lessened mitochondrial crista and smaller shrunken mitochondria. Similarly, the Perl's Prussian blue (PPB) staining also revealed a higher accumulation of iron in the liver affected by HIRI compared to the sham and ACT groups (Fig. 2C). Accordingly, the levels of Fe^{3+} and Fe^{2+}, and the contents of MDA and 4-Hydroxynonenal (4-HNE) in mice liver were much higher in HIRI groups but decreased after treated with different dosages of ACT, suggesting the restrained iron accumulation and oxidative stress in liver (Fig. 2D). It has been reported that GPX4 and transferrin function as regulatory proteins of hepatic iron metabolism and play crucial roles in the progression of ferroptosis[19]. As expected, the protein levels of GPX4 and transferrin were downregulated in the HIRI group but remarkably upregulated following ACT treatment (Fig. 2E and Fig. S2B). Considering that the main cell cluster damaged by HIRI in the liver was hepatocyte, we established an *in vitro* HR system in parallel with HIRI environment or treated with erastin (a ferroptosis inducer) in AML 12 cells (mouse liver cell line). As shown in Fig. 2F and G, Fig. S2C and S2D, we found the anabatic apoptosis (marked by red immunofluorescence in TUNEL images) of hepatocytes in both HR- and erastin-induced AML 12 cells, which were inhibited to varying degree in ACT groups (25, 50 and 100 μmol/L) or Fer-1. Meanwhile, the cytoplasmic iron deposition of hepatocytes (indicated by blue spots) exhibited a significant increase in both HR- and erastin-stimulated groups, whereas ACT led to a reduction in the extent of blue depositional region. Besides, the Mito-Tracker red fluorescence staining revealed the rescued mitochondrial membrane potential in different ACT and Fer-1 groups. Moreover, the levels of Fe^{3+} and Fe^{2+}, and the contents of MDA and 4-HNE in AML 12 cells were also enhanced under HR or erastin insult but significantly decreased after ACT or Fer-1 treatments (Fig. 2H and I), which were consistent with the increased protein level of GPX4 and transferrin in AML 12 cells (Fig. S2E and S2F). In addition, we also detected the changes of GPX4 under the RSL3 (an GPX4 inhibitor and ferroptosis activator), ACT or fer-1 treatments, and found that ACT and fer1-1 upregulated both mRNA and protein levels of GPX4 (Fig. S2G and S2H). Overall, these findings suggested that the ferroptosis effects induced by HIRI primarily destroy hepatocytes, and ACT can effectively inhibit this process.

3.3. ACT effectively increases PCBP2 in hepatocytes with ischemia and hypoxia damage

To investigate the genes implicated in ferroptosis during HIRI progression, RNA-seq analysis was conducted on liver samples from sham, HIRI and HIRI + ACT groups. A total of 51 ferroptosis-related genes were identified, primarily enriched in pathways related to chaperonin, ion transport, intercellular lipid metabolism, and cell proliferation. Especially, among those DEGs, *Pcbp2* was dramatically downregulated in the HIRI group but significantly upregulated after ACT treatment (Fig. 3A). To further elucidate the role of PCBP2 in the ferroptosis during HIRI, subsequent validations were conducted using qPCR, Western blot and immunofluorescence. As shown in Fig. 3B and C and Supporting Information Fig. S3A−S3C, the expression of PCBP2 in HIRI livers was markedly reduced than that in the sham group but significantly enhanced after ACT treatment, suggesting that ACT may achieve its protective effects on HIRI by targeting PCBP2. Considering that hepatocytes might be the primary target cell population subject to HIRI, we then isolated the primary hepatocytes and further performed RNA sequencing of this single cell type. As expected, from the volcano plots analysis of isolated primary hepatocytes, *Pcbp2* was also significantly downregulated in hepatocytes under HIRI insult but upregulated after ACT

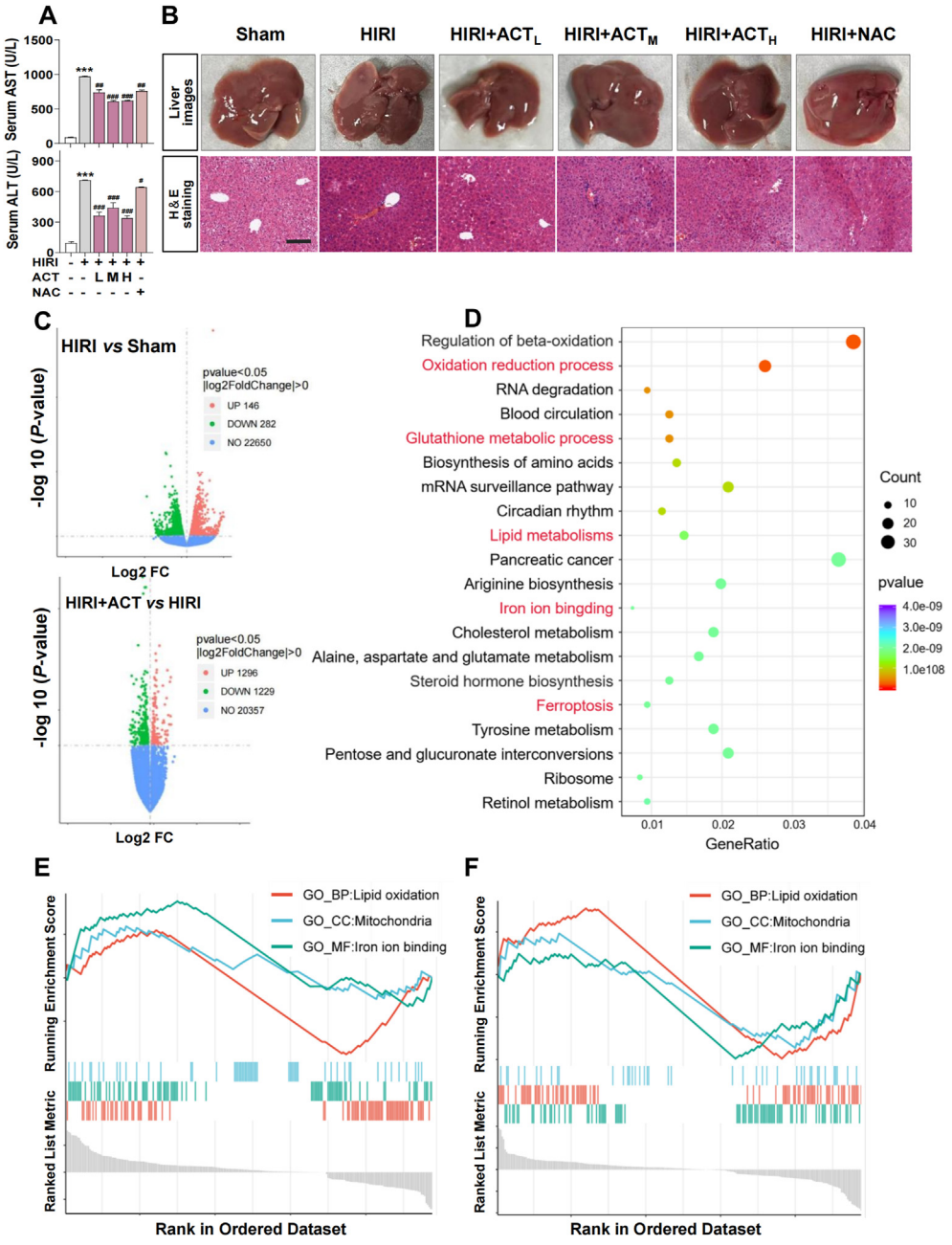

Figure 1 ACT alleviates HIRI-induced hepatic injury by inhibiting ferroptosis. (A) Serum AST and ALT levels. Statistical significance: $^{***}P < 0.001$, compared with control groups; $^{\#}P < 0.05$, $^{\#\#}P < 0.01$, $^{\#\#\#}P < 0.001$, compared with model groups ($n = 6$). (B) Liver images and H & E images, scale bar = 40 μm. (C) The volcano plot of gene set in HIRI group *vs* Sham group and HIRI + ACT group *vs* HIRI group. (D) The bubble diagram of the enriched pathway of significantly changed genes in Sham, HIRI and HIRI + ACT group. The GSEA analysis of (E) HIRI group *vs* Sham group and (F) HIRI + ACT group *vs* HIRI group.

treatment (Fig. 3D). Similarly, the changes of mRNA and protein expression of PCBP2 in AML 12 cells treated with different stimulators and ACT were in accordance with that in RNA sequencing data from hepatocytes only (Fig. 3E and F, Fig. S3D). Notably, the increased production of ROS triggered by HR or erastin might be connected with the reduction in the presence of PCBP2, a phenomenon that was fully restored with ACT treatment at varying doses (Fig. 3G and H, Fig. S3E and S3F). These results suggested that PCBP2 appeared to be an important but silent anti-ferroptosis target during HIRI, which may be reawakened by ACT.

3.4. ACT assists PCBP2 to maintain the system Xc$^-$ and further restrain hepatocyte ferroptosis

As a reported RNA-binding protein, the regulation of PCBP2 on SLC7A11 (the light chain of system Xc$^-$) has been studied preliminarily[9], while the regulatory role of PCBP2 in the expression of SLC3A2 and the entire system Xc$^-$ requires further investigation. We then explored the underlying mechanism about how PCBP2 regulated the system Xc$^-$, and we found that *Slc3a2* and *Slc7a11* were positively correlated with *Pcbp2* by analyzing the

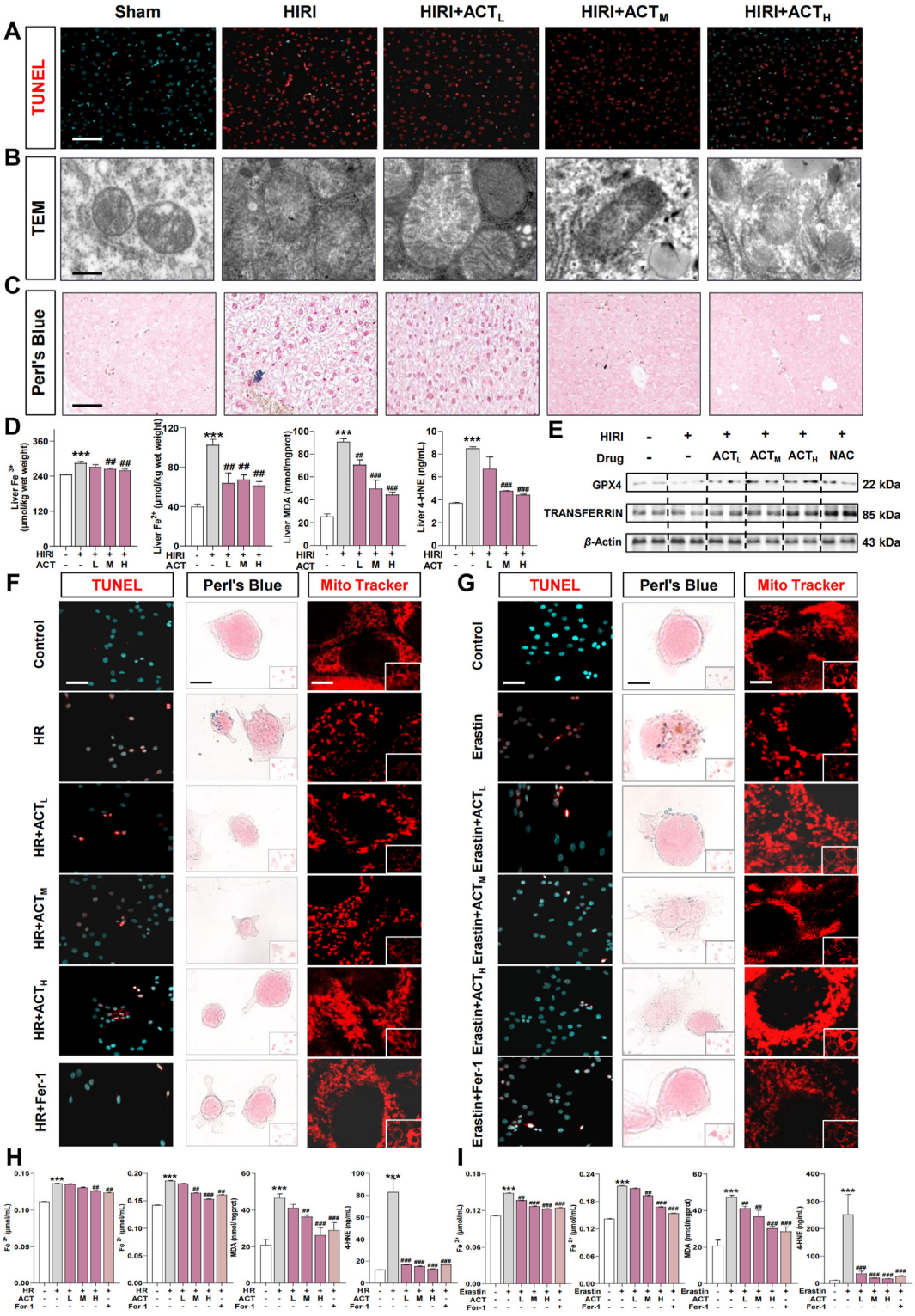

Figure 2 ACT inhibits hepatocyte ferroptosis both *in vivo* and *in vitro*. (A) Representative images of TUNEL immunofluorescence staining of mice liver, scale bar = 40 μm. (B) Representative images of TEM in the mouse liver, scale bar = 5 nm. (C) Representative images of PPB staining in the mouse liver, scale bar = 40 μm. (D) The content of Fe^{3+}, Fe^{2+}, MDA and 4-HNE in mice liver. Statistical significance: $^{***}P < 0.01$, compared with relative control groups; $^{\#\#}P < 0.01$, $^{\#\#\#}P < 0.001$, compared with relative model groups ($n = 6$) (E) The protein levels of GPX4 and transferrin were measured by Western blot and normalized by β-actin in the mice liver. Representative images of TUNEL immunofluorescence staining, PPB staining and Mito-Tracker red fluorescence staining in the AML 12 cells under (F) HR and (G) erastin insult, scale bar = 100 μm. The contents of Fe^{3+}, Fe^{2+}, MDA and 4-HNE in AML 12 cell under (H) HR and (I) erastin insult. Statistical significance: $^{***}P < 0.01$, compared with relative control groups; $^{\#\#}P < 0.01$, $^{\#\#\#}P < 0.001$, compared with relative model groups ($n = 6$).

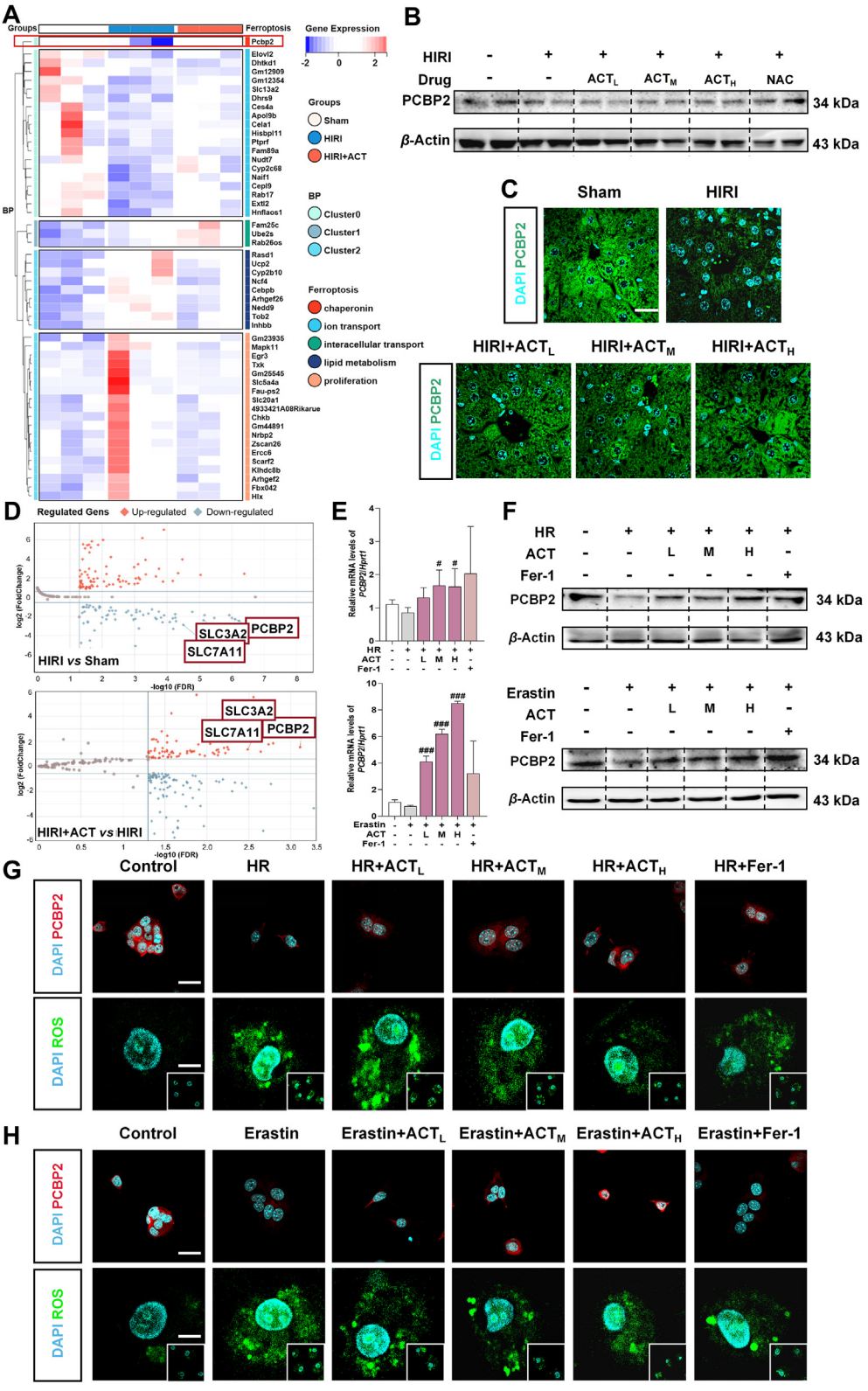

Figure 3 ACT upregulates the expression of PCBP2 *in vivo* and *in vitro*. (A) The heatmap of ferroptosis-related genes of mice liver. (B) The protein levels of PCBP2 were measured by Western blot and normalized by β-actin in mice liver. (C) Representative images of PCBP2 staining in the mouse liver, scale bar = 40 μm. (D) The volcano plot of ferroptosis-related genes in hepatocytes. (E) Relative mRNA levels of *Pcbp2* in AML12 cells were measured by qPCR and further normalized with *hprt1*. Statistical significance: $^{\#}P < 0.05$, $^{\#\#\#}P < 0.001$, compared with relative model groups ($n = 6$). (F) The protein levels of PCBP2 were measured by Western blot and normalized by β-actin in the AML 12 cells. (G, H) Representative images of PCBP2 and ROS staining in the AML12 cells under HR or erastin insult, scale bar = 100 μm.

gene correlations of *Pcbp2* and *Slc3a2*/*Slc7a11* from gene maps of mice liver and hepatocytes (Fig. 4A), which was supported by the higher mRNA levels and protein levels of *Pcbp2*, *Slc3a2*, *Slc7a11* and system Xc^-- regulated *Gpx4* of the liver in ACT groups (Fig. 4B and C, Supporting Information Fig. S3A and S4A). Besides, the co-expression changes of SLC3A2 and SLC7A11 across various groups were validated by immunofluorescence stain7ng. Again, ACT promoted the co-localization of the light chain and heavy chain of system Xc^- in livers (Fig. 4D). Additionally, the contents of Cys and GSH (synthesized by glycine) in livers were detected to observe the cystine-glycine transportation function of system Xc^-, and Fig. 4E shows that the function of system Xc^- was also inhibited under HIRI insult, which could be largely improved by ACT administration. Moreover, the *in vivo* results have been further validated on hepatocytes, both qPCR and Western blot analysis revealed that HR and erastin significantly downregulated the expression of SLC3A2 and SLC7A11 (The target SLC7A11 showed a better trend), which were subsequently markedly upregulated by ACT (Fig. 4F and G, Fig. S4B). Fig. 4H and quantized image histogram (Fig. 4I) further confirmed the enhanced intensity of co-expression of SLC3A2 and SLC7A11 after ACT or fer-1 treatments compared to HR or erastin stimulation. Correspondingly, ACT and fer-1 also evidently increased the contents of Cys and GSH in hepatocytes, thereby repairing the ferroptosis-related redox imbalance (Fig. 4J). These results suggested that damaged system Xc^- under hypoxia condition was positively correlated with the inhibition of PCBP2 and was largely reversed by ACT, but this specific protection mechanism required further in-depth exploration.

3.5. *ACT promotes PCBP2 to directly bind to and maintain the stability of system Xc^- in hepatocytes*

After confirming the potential binding sites of PCBP2 and ACT (Supporting Information Fig. S5A), we applied the SPR experiment and found that ACT could interact with PCBP2 protein in a dose-dependent manner, with the determined equilibrium dissociation constant (K_D) at 0.3117 μmol/L (Fig. 5A). Besides, MST was performed with increasing concentrations of ACT and a certain amount of PCBP2 protein (10 μmol/L), which showed the incremental ACT significantly affect the thermophoretic motion of PCBP2 protein, with K_D values of 1.4 ± 0.18 μmol/L (Fig. 5B). These results suggested that ACT could directly bind to the PCBP2. To further elucidate the regulatory impact of ACT on the interaction between PCBP2 and system Xc^- in the progression of HIRI, we employed the commonly used protein−protein docking engines, ZDOCK, to simulate the predicted docking complexes of PCBP2 (AlphaFoldDB: Q61990) and SLC3A2 (PDB: 6I9Q Chain A)/SLC7A11 (AlphaFoldDB: Q61990). The binding free energy and potential interacting residues were then calculated and visualized. The listed docking score (−13.076, −73.13 kcal/mol for PCBP2−SLC3A2; −7.727, −46.41 kcal/mol for PCBP2-SLC7a11) showed the negative binding free energy and highly docking stability of PCBP2−SLC3A2 and PCBP2−SLC7A11 (Figs. S5B−S5D). Then, we generated accurate models of the protein−protein complexes for subsequent molecular docking analysis. PRO156 and SER297 might form the hydrophobic interactions in the hydrophobic pocket of ACT and PCBP2−SLC3A2 complexes (Fig. 5C), with the SER 301 and TYR 241 forming the hydrogen bonds in ACT and PCBP2−SLC7A11 complexes (Fig. 5D). Meanwhile, the co-IP experiments were conducted to confirm that SLC3A2 and SLC7A11 positively bind with PCBP2 and ACT could strengthen the protein combination between PCBP2 and system Xc^- (Fig. 5E). Furthermore, multiplex immunohistochemical staining showed that the co-localization of PCBP2, SLC3A2 and SLC7A11 was broken down under HIRI insult but was improved by ACT treatment (Fig. 5F and Fig. S5E).

In addition to the influence on the protein binding of PCBP2 and system Xc^-, we also speculated that the ACT could also regulate the mRNA stability of PCBP2 and system Xc^- for further disturbing their expressions. We then predicted the interactions of PCBP2 (the RBP) and *Slc3a2*/*Slc7a11* (the mRNA) by CLIP-seq database (starBase: https://rnasysu.com/encori/index.php). Fig. S5F shows that the mRNA levels of *Slc3a2* and *Slc7a11* were positively and markedly regulated by PCBP2. Consistently, the administration of ACT markedly increased the mRNA stability of *Pcbp2*, *Slc3a2* and *Slc7a11* at 1, 4 and 2 h, respectively (Fig. S5G). For clearly figuring out the regulatory role of PCBP2 on system Xc^- and therapeutic mechanism of ACT, the si-PCBP2 was used in the AD assay for verifying the mRNA stability of system Xc^- at this stimulation. Our results revealed that although the mRNA stabilities of *Slc3a2* and *Slc7a11* were compromised after PCBP2 knockdown, ACT still increased these gene expressions to some extent (Fig. 5G). In more detail, the mRNA and protein levels of PCBP2, SLC3A2 and SLC7A11 were downregulated by si-PCBP2 but were increased either by ACT or ferroptosis inhibitor (Fig. 5H and I, Fig. S5H). Following transfection with si-PCBP2, hepatocytes displayed heightened susceptibility to ferroptosis attributed to a reduction in Cys levels, alongside a notable oxidative stress as indicated by elevated MDA content and decreased SOD activity, which were all improved by ACT (Fig. 5J). The findings indicated that PCBP2 played a critical role in stabilizing SLC3A2 and SLC7A11, potentially providing a binding pocket that interacts with ACT to inhibit ferroptosis in a manner dependent on PCBP2.

3.6. *ACT restrained HMGB1 secretion by promoting PCBP2 to inhibit p300 activity in ferroptotic hepatocytes*

Previous study has demonstrated that autocrine or paracrine DAMPs are released following cell ferroptosis, thereby exacerbating the progression of HIRI[20]. We noticed the enrichment of DAMPs-related pathways (Toll like receptors signaling, RIG-I protein signaling and HSP90 chaperone cycle pathway) at first (Fig. 6A). After conducting an analysis on the DEGs associated with DAMPs, we observed a significant upregulation of HMGB1 among these gene candidates, which exhibited a significant correlation with *Pcbp2* (Fig. 6B). Consistently, the elevated hepatic expression and secretion of HMGB1 under hypoxic environment were observed both *in vivo* and *in vitro*, which were largely inhibited after ACT or fer-1 intervention (Fig. 6C and Supporting Information Fig. S6A). Generally, the nuclear export and exocytosis release of HMGB1 required the lactic modification of HMGB1, which can be facilitated by the histone acetyltransferase p300[21,22]. As transcriptional coactivators of multiple sequence-specific transcription factors, CREB-binding protein (CBP) and p300 facilitated the transcriptional activity of hypoxia-inducible factor 1α (HIF1α) under the HIRI process[23,24]. Interestingly, the correlation between PCBP2 and HIF1α or p300 or HMGB1 exhibited significant relevance in the CLIP data analysis, respectively (Fig. 6D). Subsequently, qPCR assay exhibited that HR, erastin or si-PCBP2 could upregulate the mRNA level of *hif1α*. Meanwhile, si-PCBP2 and CTB (a p300 activator) could elevate the gene and protein expressions of p300 and HMGB1, which

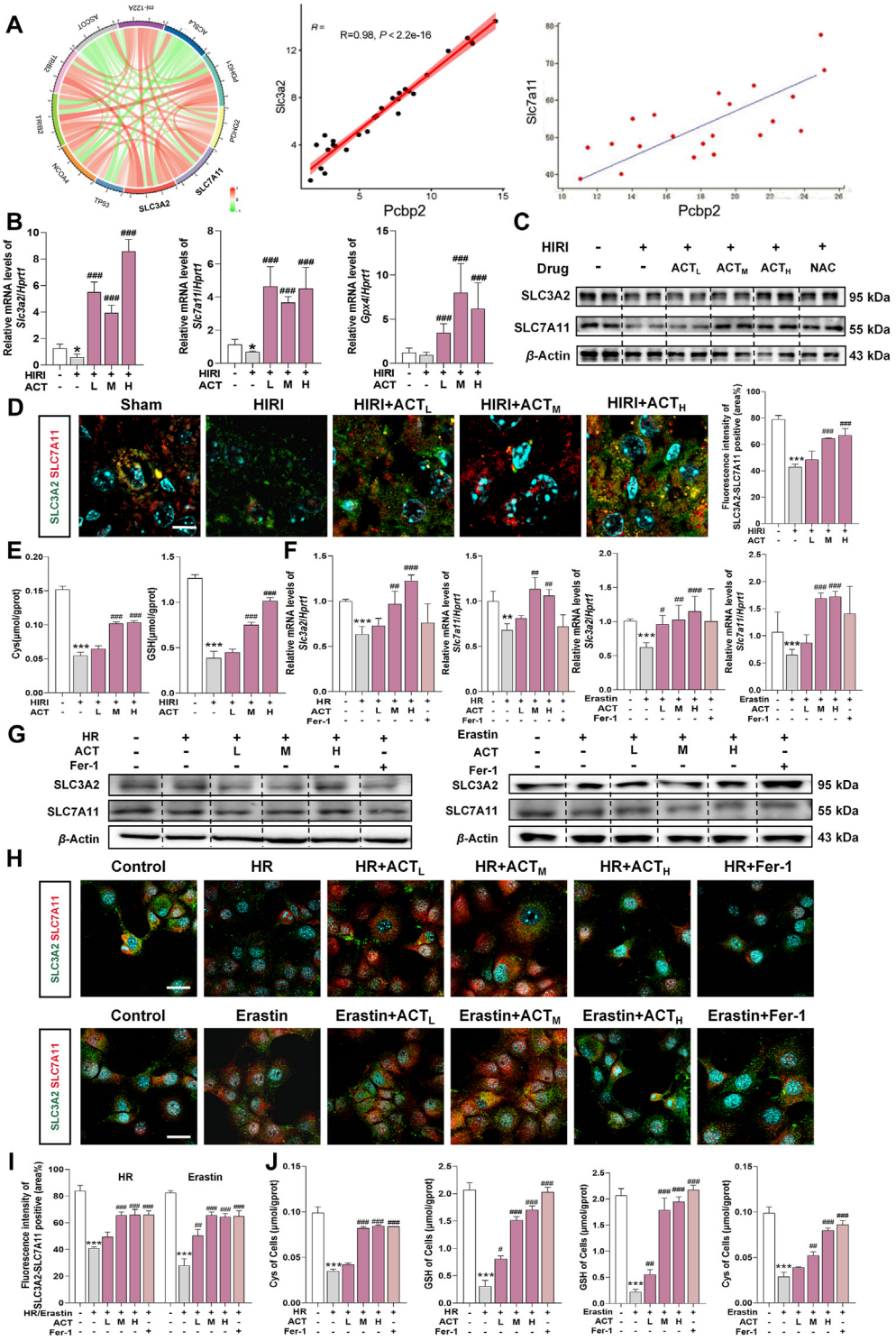

Figure 4 ACT improves the expression and function of the System Xc^- under hypoxia conditions. (A) The circle chart (left panel, whole livers RNA-sequence data) and coefficient chart (middle and right panel, only hepatocytes RNA-sequence data) for the relationship between PCBP2 and SLC3A2/SLC7A11. (B) Relative mRNA levels of *Slc3a2*, *Slc7a11* and *Gpx4* in mouse livers were measured by qPCR and further normalized with *hprt1*. Statistical significance: $^{*}P < 0.05$, compared with relative control groups; $^{\#\#\#}P < 0.001$, compared with the relative model groups ($n = 6$). (C)The protein levels of SLC3A2 and SLC7A11 were measured by Western blot and normalized by β-actin in mouse livers. (D) Representative images of SLC3A2 and SLC7A11 staining in the mouse liver, scale bar = 40 μm. Statistical significance: $^{***}P < 0.001$, compared with relative control groups; $^{\#\#\#}P < 0.001$, compared with the relative model groups ($n = 6$). (E) The content of Cys and GSH in mice liver. Statistical significance: $^{***}P < 0.001$, compared with relative control groups; $^{\#\#\#}P < 0.001$, compared with the relative model groups ($n = 6$). (F) Relative mRNA levels of *Slc3a2* and *Slc7a11* in AML 12 cells were measured by qPCR and further normalized with *hprt1*. Statistical significance: $^{**}P < 0.01$, $^{***}P < 0.001$, compared with relative control groups; $^{\#}P < 0.05$, $^{\#\#}P < 0.01$, $^{\#\#\#}P < 0.001$, compared with the relative model groups.

partially counteracted the inhibitory effect of ACT on these targets (Fig. 6E and F, Fig. S6B and S6C). Moreover, the immunofluorescence analysis revealed that p300 activation promoted the nuclear export of HMGB1, as evidenced by the colocalization of p300 (green) and HMGB1 (red). Conversely, the upregulations of p300 and HMGB1 were inhibited in the presence of ACT or Fer-1 (Fig. 6G and Fig. S6D). These results indicated that the transcriptional activity of HIF1α induced by CBP/p300 and subsequent HMGB1 secretion were triggered due to the inhibition of PCBP, which might also be the key target for ACT to exert its protective effect.

3.7. *ACT restricted M1 macrophage recruitment by limiting the release of HMGB1 from ferroptotic hepatocytes*

Given the critical role of ferroptosis in immune responses, our analysis focused on the cell types affected by liver ferroptosis. Through Cell Marker 2.0 analysis, we identified macrophages as the most prominent immune cells under HIRI stimulation, particularly in response to HMGB1 stimulation (Fig. 7A). Besides, the marker genes of different immune cells (*F4/80*, *Cd11b* and *Cd68* for macrophages, *Cd44*, *Cd62l* and *Ly6g* for neutrophils, *Cd56*, *Cd16* and *Cxcr6* for NK cells) showed that, in comparison to the sham group, HIRI surgery significantly upregulated the expression of genes associated with M1 polarized macrophages in mice, which could be subsequently downregulated following ACT administration (Fig. 7B and Supporting Information Fig. S7A). Moreover, the flow cytometry analysis of mouse liver further revealed an increase in the population of M1 macrophages (marked by CD11b and CD11c) after HIRI insult, which could be alleviated by ACT in different doses (Fig. 7C and Fig. S7B). We further treated mouse macrophages (RAW 264.7 cells) either with conditioned medium (CM) from HR- or erastin-treated hepatocytes, as well as with HMGB1, to investigate whether HMGB1 released from ferroptotic hepatocytes influences macrophage phenotype and function. Accordingly, all the M1 macrophage genes (marked by *Il1b*, *Il6* and *Inos*) but not M2 genes (*Il10* and *Il4*) were increased to different degrees under the CM from HR- or erastin-hepatocytes (Fig. 7D) and HMGB1 stimulation (Fig. 7E), which were decreased after ACT administration. In addition, the transwell assay was utilized to evaluate macrophage migration, demonstrating that CM from both HR- and erastin-treated hepatocytes significantly enhanced macrophage recruitment (Fig. 7F). The similar effects of CM from HR- and erastin-treated hepatocytes on the activation and recruitment of M1 macrophages were also observed in THP-1 cells (Fig. S7C and S7D).

Furthermore, the $GdCl_3$ (10 mg/kg) was administered to eliminate macrophages for observing the paracrine function of hepatocyte-derived HMGB1 on macrophages. We found that the combination of ACT (50 mg/kg) and $GdCl_3$ not only alleviated the liver function and hepatic pathological damage, but also inhibited the mRNA levels of M1 macrophages markers (*F4/80*, *Cd11b*, *Il6* and *Inos*) but not HMGB1 and M2 markers in HIRI mice (Supporting Information Fig. S8A–S8C). These findings suggested that macrophage enhancement and recruitment occurred during liver ferroptosis, possibly triggered by HMGB1 secretion from ferroptotic hepatocytes and mitigated by ACT or fer-1 treatments.

3.8. *Hepatocyte specific knockdown of PCBP2 can partially antagonize the hepatoprotective effect of ACT*

To further substantiate the involvement of PCBP2-mediated hepatic ferroptosis in HIRI, the si-PCBP2 was packed in the well-sized LNPs labeled by the ApoE protein to target hepatocytes according to the reported studies[25,26]. As shown in TEM images (Supporting Information Fig. S9A) and particle–size graph (Fig. 8A), the LNPs-si-PCBP2 were detected as monodispersed spherical nanoparticles with the average diameter of 83.91 nm. Besides, the zeta potential and encapsulation percentage (EE%) of LNPs-si-PCBP2 were 6.81 mV and 84.33%, respectively (Fig. 8B, Fig. S9B and S9C). Moreover, the long-term stability of LNPs-si-PCBP2 was verified in PBS and serum. The hydrodynamic diameters of LNPs-si-PCBP2 remained unchanged, suggesting the evident stability of LNPs-si-PCBP2 in different solutions (Fig. 8C). LNPs-si-PCBP2 also exhibited a cumulative release of si-PCBP2 until 120 h, meanwhile the free siRNA showed a quick release in 6 h (Fig. 8D).

To assess the targeting effects of LNPs-si-PCBP2 on mice liver, we tail-intravenously injected the dyestuff DIR and DIR labeled LNPs-si-PCBP2 into the mice. As shown in Fig. S9D and S9E, the obvious fluorescence signals were observed and almost accumulated in liver at 6 h in the DIR labeled LNPs-si-PCBP2 mice. We further administered the LNPs-si-PCBP2 intravenously *via* the caudal vein prior to HIRI surgery and ACT pre-administration in mice (Fig. 8E). Herein, the contents of iron ion (Fe^{3+} and Fe^{2+}), ROS, LPO and MPO in liver were increased, the level of Cys in the liver and the GSH in serum and liver were decreased in HIRI plus LNPs-si-PCBP2 group and HIRI plus LNPs-si-PCBP2 plus ACT group (Fig. 8F and S9F). Histological examination (Fig. 8G and S9G) indicated that the degree of liver tissue injury was exacerbated under injected with LNPs-si-PCBP2, which were only partially alleviated by ACT treatment. In addition, compared with HIRI liver, LNPs-si-PCBP2 increased the iron deposition area as indicated by PPB staining, which was not completely inhibited by ACT administration (Fig. 8H). Moreover, the multi-color fluorescence results showed the decreased co-expression of PCBP2 and system Xc^- after silencing PCBP2 in hepatocytes, which were then mitigated to some extent by ACT (Fig. 8I, Fig. S9H and S9I). Accordingly, in comparison to the HIRI mice, the injection of LNPs-si-PCBP2 markedly upregulated the fluorescence intensity of HMGB1 and CD68 (a typical cell marker for macrophages) in livers, and simultaneously, which was only partly decreased with the presence of ACT (Fig. 8J and K, Fig. S9J and S9K). Besides, as shown in Fig. 8L and Fig. S9L, the mRNA expressions of *pcbp2*, *slc3a2* and *slc7a11* in HIRI plus LNPs-si-PCBP2 mouse liver were downregulated than that in the sham and HIRI group, while ACT could not significantly upregulate *pcbp2* and system Xc^- related genes under the si-PCBP2 intervention. Meanwhile, referred to sham and HIRI groups for comparison, the mRNA levels of *p300*, *hmgb1* and *F4/80* were significantly increased by the transfection of si-PCBP2, which notably, were no longer reversed by ACT pretreatment as before. Overall, the reversal of therapeutic effects of ACT on HIRI mice can be directly linked to the knockdown of hepatocyte-specific PCBP2.

(G) The protein levels of SLC3A2 and SLC7A11 were measured by Western blot and normalized by β-actin in AML 12 cells. (H) Representative images of SLC3A2 and SLC7A11 staining in the AML 12 cells, scale bar = 100 μm. (I) The quantization chart for SLC3A2 and SLC7A11 staining in AML 12 cells. (J) The content of Cys and GSH in AML 12 cells. Statistical significance: $^{***}P < 0.001$, compared with relative control groups; $^{\#}P < 0.05$, $^{\#\#}P < 0.01$, $^{\#\#\#}P < 0.001$, compared with the relative model groups.

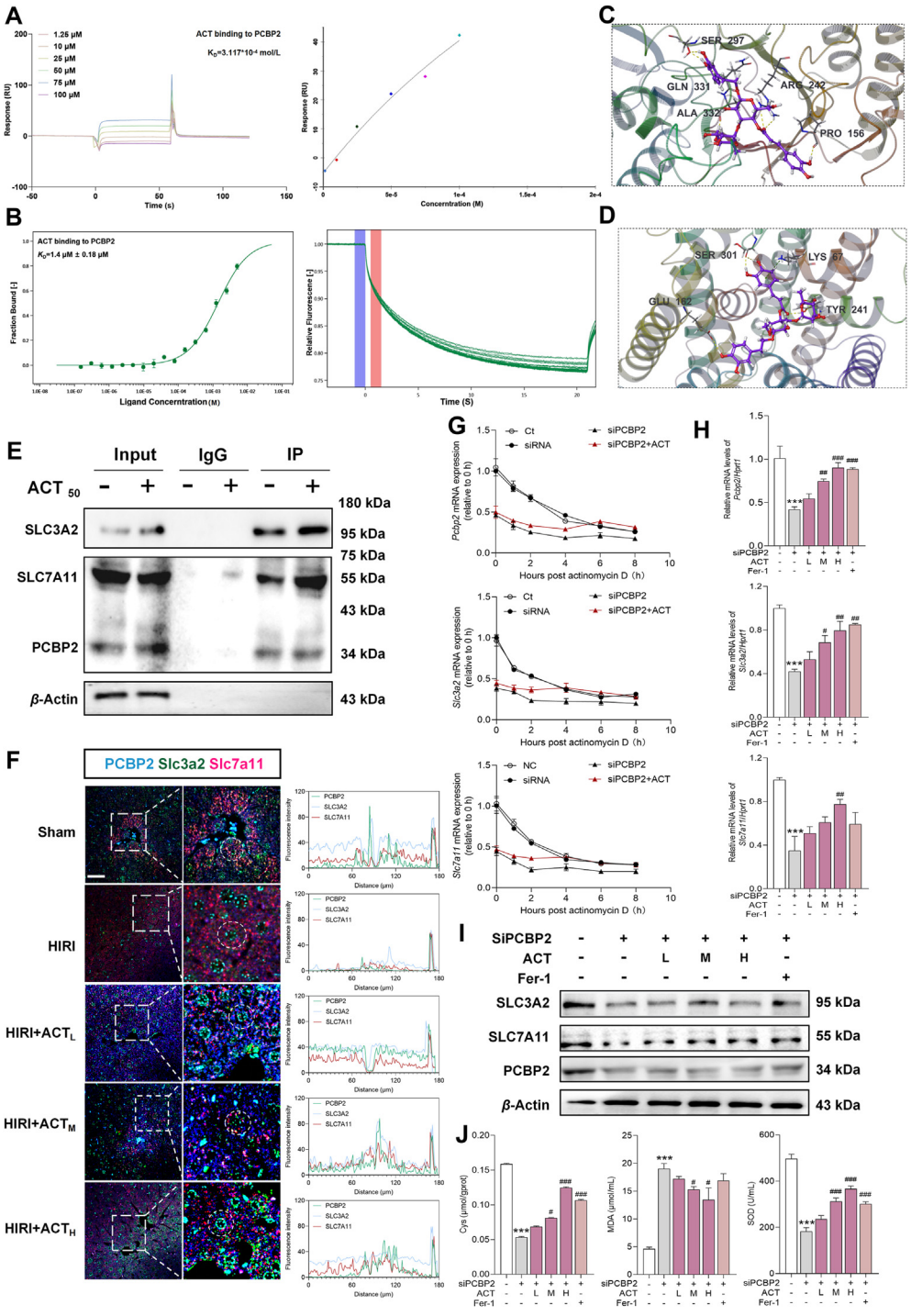

Figure 5 ACT promotes PCBP2 to maintain the stability of system Xc^{-}. (A) The SPR detection of ACT with PCBP2 protein. (B) The MST results of ACT with PCBP2 protein. (C) The molecular simulation docking between ACT and PCBP2−SLC3A2 protein complex. (D) The molecular simulation docking between ACT and PCBP2−SLC7A11 protein complex. (E) The co-IP results between PCBP2 and SLC3A2/SLC7A11. (F) The representative images of multi-color fluorescence staining of PCBP2/SLC3A2/SLC7A11 in mouse livers, scale bar = 40 μm. (G) The mRNA changes of *Pcbp2*, *Slc3a2* and *Slc7a11* in hepatocytes. (H) Relative mRNA levels of *Slc3a2*, *Slc7a11* and *PcBP2* in AML12 cells were measured by qPCR and further normalized with *hprt1*. Statistical significance: $^{***}P < 0.001$, compared with control group; $^{\#}P < 0.05$, $^{\#\#}P < 0.01$, $^{\#\#\#}P < 0.001$, compared with the siPCBP2 group ($n = 3$). (I) The protein levels of PCBP2, SLC3A2 and SLC7A11 were measured by Western blot and normalized by β-actin in AML 12 cells. (J) The content of Cys, MDA and SOD in AML 12 cells. Statistical significance: $^{***}P < 0.001$, compared with control group; $^{\#}P < 0.05$, $^{\#\#\#}P < 0.001$, compared with the siPCBP2 group ($n = 3$).

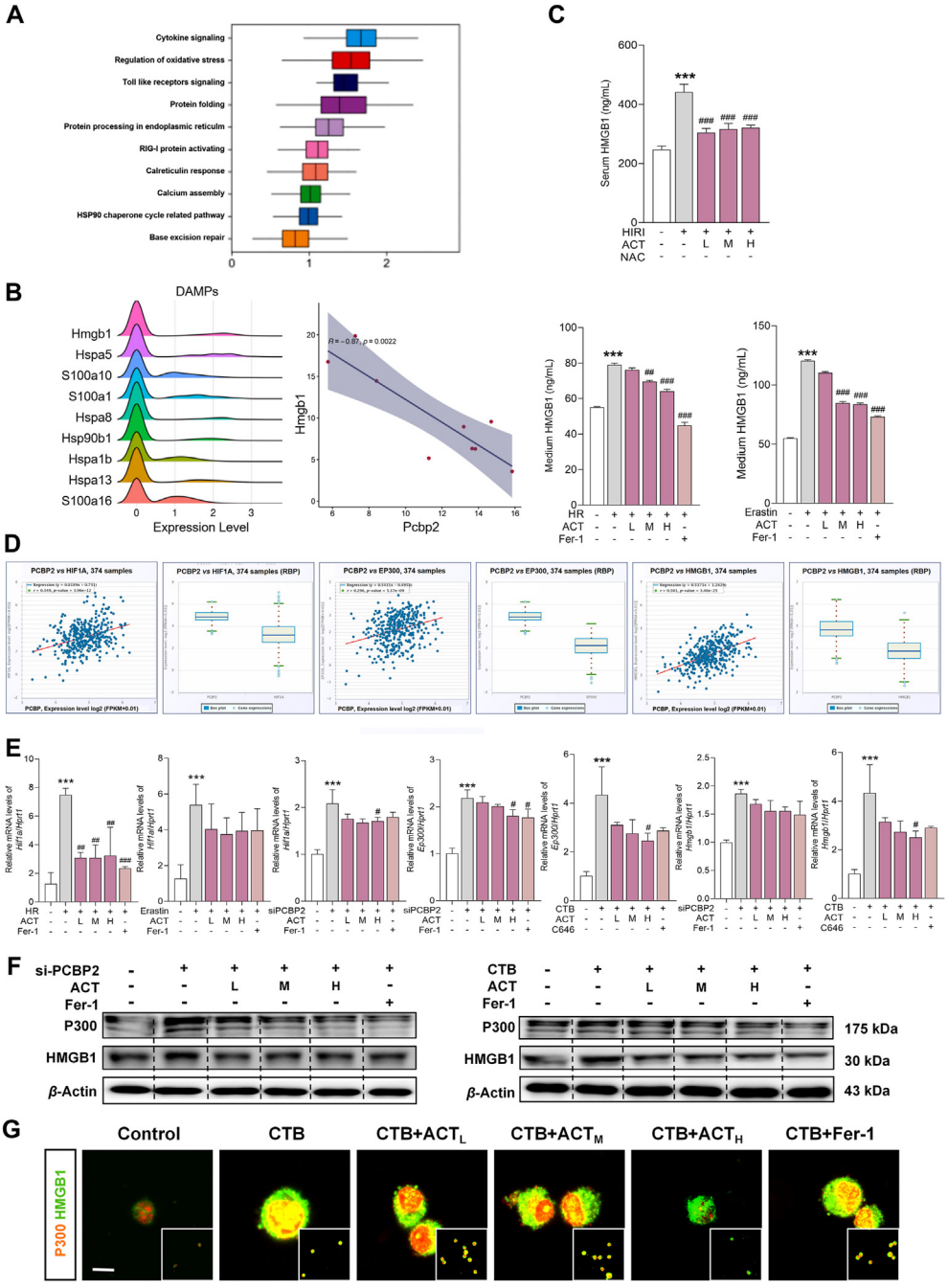

Figure 6 ACT upregulates PCBP2 to inhibit the P300/HIF1α/HMGB1 signaling in hepatocytes. (A) The diagram of pathway enrichment analysis. (B) The ridgeline plot (left) of DAMPs related genes and the coefficient diagram (right) of HMGB1 and PCBP2. (C) The level of HMGB1 in mouse serum and AML 12 cell medium. Statistical significance: $^{***}P < 0.001$, compared with the control group; $^{\#\#}P < 0.01$, $^{\#\#\#}P < 0.001$, compared with the relative model groups ($n = 6$). (D) The RBP-mRNA CLIP results of PCBP2−HIF1α, PCBP2−P300 and PCBP2−P300. (E) The mRNA changes of *Hif1a*, *Ep300* and *Hmgb1* in AML12 cells were measured by qPCR and further normalized with *hprt1*. Statistical significance: $^{***}P < 0.001$, compared with the control group; $^{\#}P < 0.05$, $^{\#\#}P < 0.01$, $^{\#\#\#}P < 0.001$, compared with the relative model groups ($n = 3$). (F) The protein levels of P300 and HMGB1 were measured by Western blot and normalized by β-actin in AML 12 cells. (G) The representative images of P300 and HMGB1 staining in AML 12 cells, scale bar = 100 μm.

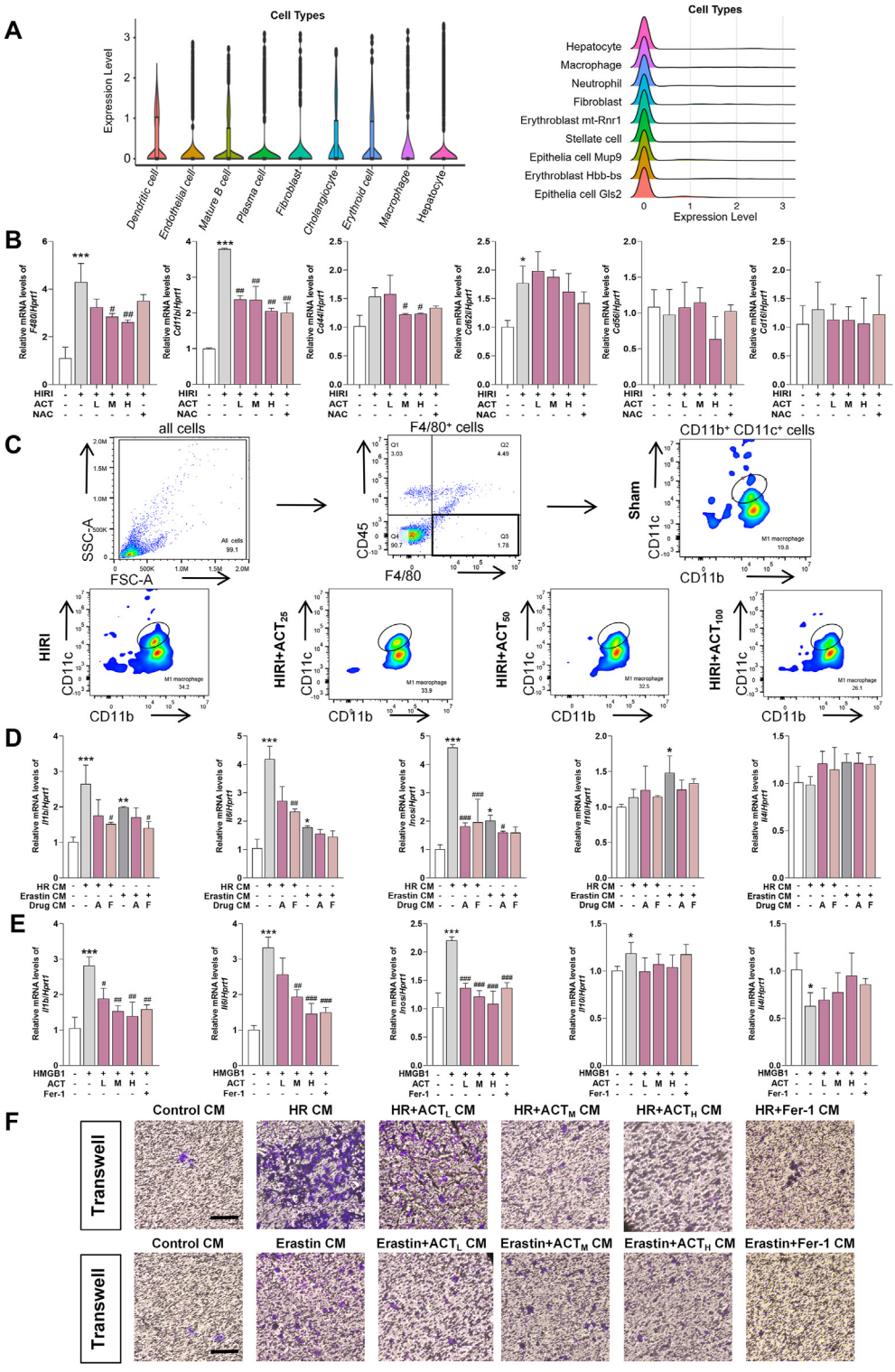

Figure 7 ACT restrains the activation and recruitment of macrophages by inhibiting the HMGB1 released from hypoxic hepatocytes. (A) The diagram (left) and ridgeline plot (right) of cell cluster in gene set from mouse livers. (B) Relative mRNA levels of *F4/80*, *Cd11b*, *Cd44*, *Cd62l*, *Cd56* and *Cd16* in mouse livers were measured by qPCR and further normalized with *hprt1*. Statistical significance: $^{*}P < 0.05$, $^{***}P < 0.001$, compared with relative control groups; $^{\#}P < 0.05$, $^{\#\#}P < 0.01$, compared with relative model groups ($n = 6$). (C) The flow cytometry of primary macrophages isolated from mice. Relative mRNA levels of *Il1b*, *Il6*, *Inos*, *Il10*, and *Il4* in (D) CM- or (E) HMGB1 recombinant protein-treated RAW 264.7 cells were measured by qPCR and further normalized with *hprt1* (Drug CM: Drug A, ACT 50 μmol/L; Drug F, Fer-1) Statistical significance: $^{*}P < 0.05$, $^{***}P < 0.001$, compared with relative control groups; $^{\#}P < 0.05$, $^{\#\#}P < 0.01$, $^{\#\#\#}P < 0.001$, compared with relative model groups ($n = 3$). (F) The representative transwell images of RAW 264.7 cells. Scale bar = 100 μm.

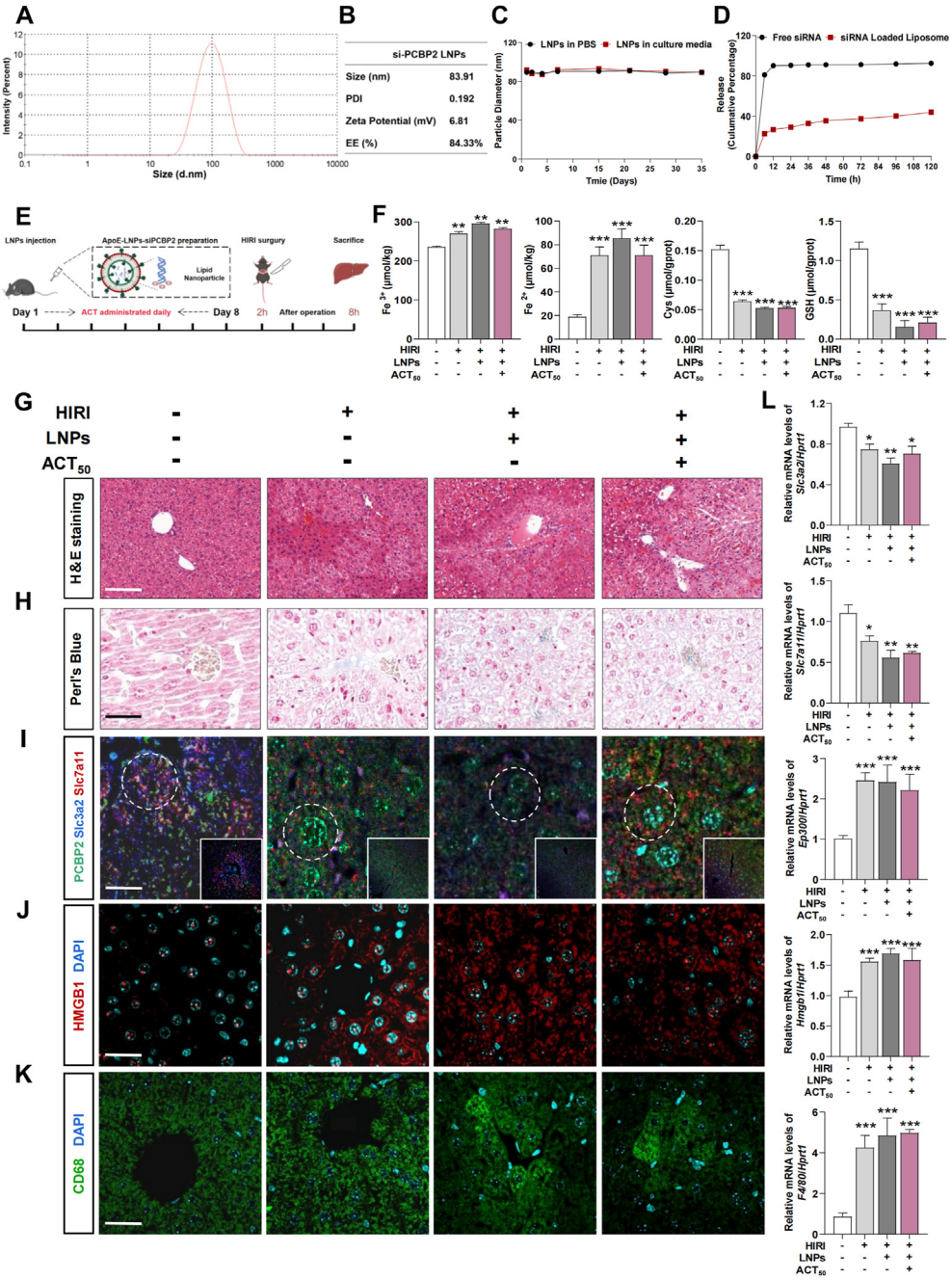

Figure 8 The hepatocyte specific knockout of PCBP2 interferes the therapeutic effects of ACT. (A) The particle size, (B) PDI, zeta potential and EE (%) of LNPs-si-PCBP2. (C) The stability of LNPs-si-PCBP2 in PBS and cell culture media. (D) The release behaviors of free si-RNA and LNPs-si-PCBP2. (E) Flow chart of ApoE-LNPs animal experiment. (F) The content of Fe $^{3+}$, Fe $^{2+}$, Cys and GSH in mouse livers. Statistical significance: $^{**}P < 0.01$, $^{***}P < 0.001$, compared with the sham group ($n = 6$). Representative images of (G) H & E staining (scale bar = 40 μm), (H) PPB staining (scale bar = 40 μm), (I) immunofluorescence staining for PCBP2/SLC3A2/SLC7A11 (scale bar = 40 μm), (J) immunofluorescence staining for HMGB1 (scale bar = 40 μm) and (K) CD68 (scale bar = 40 μm) in mouse livers. (L) The Relative mRNA levels of *slc3a2*, *slc7a11*, *p300*, *hmgb1* and *F4/80* were measured by qPCR and further normalized with *hprt1* in mouse livers. Statistical significance: $^{*}P < 0.05$, $^{**}P < 0.01$, $^{***}P < 0.001$, compared with the sham group ($n = 6$).

4. Discussion

HIRI has thus far been labeled as a nonnegligible component of liver transplantation surgery, unavoidable pathogenesis, and limiting factor for organ availability and survival rate. Recently, hepatocyte ferroptosis has emerged as a promising therapeutic target for alleviating HIRI. In this study, we identified an iron-dependent form of hepatocyte death that is characterized during the progression of HIRI in mice (Figs. 1 and 2). Then the sequencing bioinformatics of the whole mouse liver suggested that the hepatocytes ferroptosis was highly correlated with down-regulated PCBP2, which has been further evidently reverified by

the transcriptomics of primary mouse hepatocytes and cellular colocalization analysis (Fig. 3). Notably, we reported that PCBP2 contributed to maintain the intracellular and extracellular exchange of GSH and Cys by safeguarding the system Xc^-, thereby preserving the antioxidant defense of hepatocytes against HIRI insult. Furthermore, ACT was found to alleviate HIRI-induced ferroptosis by upregulating PCBP2, binding to and promoting PCBP2 to act as an RNA binding protein to maintain the stability of system Xc^- and retain the function of GSH-Cys transportation (Figs. 4 and 5). Besides, Figs. 6 and 7 supported that the inhibition of PCBP2 contributed to the secretion of hepatocytes-originated HMGB1 by upregulating HIF1α/p300 axis, which eventually promoted the activation and recruitment of M1 macrophages and subsequent inflammatory cascade during HIRI. Meanwhile, ACT also suppressed the activation of the inflammatory phenotype and recruitment of M1 macrophages through reversing above targets. Subsequently, taking the matched particle size and characteristics of ApoE-dependent uptake of hepatocytes, we constructed an ApoE-conjugated lipoplexes as the vehicle of si-PCBP2 to directly silence the *Pcbp2* in hepatocytes, and we found that the specific blockade of PCBP2 in hepatocytes could partially interfere with the mitigation of ACT on HIRI in mice (Fig. 8).

PCBP2, as a member of the ferro chaperonin family including PCBP1 and PCBP2, has always been emphasized in regulating mRNA stability and RNA binding ability[27]. PCBP2 is known to bind iron and aid in its transfer to ferritin for storage and also plays a role in modifying the mononuclear iron center through prolyl and asparagyl hydroxylases, which in turn helps regulate insulin sensitivity in liver tissues[24,28]. Additionally, PCBP2 was deemed as a potential co-chaperone of PCBP1 to regulate the acidic keto dioxygenase-1 to participate in the degradation of iron-related protease[29]. Besides, as a protein abnormally expressed during the progression of hepatocellular carcinoma, PCBP2 not only collaborated with the tribbles pseudokinase 2 to regulate the ubiquitin protease system through k48 ubiquitination, thereby providing protection against oxidative stress, but also inhibited the occurrence of ferroptosis[30-32]. Hence, PCBP2 may potentially serve as a therapeutic biomarker for hepatic injury induced by oxidative stress. Here, we initially observed a significant exacerbation of ferroptosis and oxidative stress in mice subjected to HIRI, which was closely correlated with the inhibition of PCBP2. Additionally, we observed that the natural product ACT could mitigate HIRI by significantly reducing ferroptosis in hepatocytes, inhibiting intracellular ROS production, and upregulating PCBP2 expression (Figs. 1 and 3). Of noted, the ApoE-LNPs was constructed to specifically silence PCBP2 in hepatocytes, showing a lack of inhibition on ROS production and the limitation on the therapeutic effect of ACT to alleviate HIRI (Fig. 8). Overall, PCBP2 may be a crucial target for treating HIRI but further research is warranted to elucidate other precise molecular pathways by which PCBP2 modulates hepatic ferroptosis and lipid ROS homeostasis.

System Xc^- has long been considered a key molecular mechanism in the process of ferroptosis, which is embedded on the cell membrane and consists of the dimer of SLC3A2 (the light chain) and SLC7A11 (the heavy chain), with SLC7A11 being the major functional subunit and SLC3A2 being the structural subunit[33]. The pivotal role of System Xc^- lies in the transportation of extracellular L-cystine and intracellular L-glutamate, facilitating the biosynthesis of glutathione and antioxidant defense mechanisms, thereby ensuring cellular environmental homeostasis[34]. However, the dysfunction of system Xc^- can result in ferroptosis and a decrease in GPX4 levels, which further intensifies intracellular lipid peroxidation (as indicated by ROS levels). Previous studies mainly focused on the damage of SLC7A11, as the functional protein of system Xc^- in the progression of ferroptosis, and PCBP2 has also been demonstrated to enhance the mRNA stability of SLC7A11 *via* inhibiting the ubiquitination of PCBP2 by glycerol phosphate dehydrogenase[9]. However, previous studies have not provided comprehensive insights into the regulatory role of PCBP2 in SLC3A2 within system Xc^- and its impact on the progression of HIRI, as well as the mechanism by which PCBP2 regulates these two concomitant chaperonin subunits. In this study, we first evaluated the role of PCBP2 played in maintaining the system Xc^- stability, not only in HIRI mice, but also in hepatocytes with damaged system Xc^- both induced by HR and erastin. Interestingly, molecular docking, SPR, MST and AD experiments demonstrated that ACT acted on the binding domains of PCBP2 with SLC7A11 and SLC3A2 (the active binding sites as PRO156 and TYR386) to maintain the interaction of PCBP2 and system Xc^- and the mRNA stability of *Slc7a11* and *Slc3a2* for restraining the ferroptosis in HIRI (Fig. 5). Of note, the damage of system Xc^- also negatively intervened the subsequent GPX4 to balance the oxidative stress and ferroptosis in hepatocytes, and ACT potentially regulated the stability of membrane system Xc^- transportation to protect GPX4 synthesis and following oxidative defense function (Fig. 2).

In addition to controlling the system Xc^- system, studies have also reported that PCBP2 could cooperate with PCBP1 to modify the HIF1α by activating iron-dependent proline hydroxylase and asparagine hydroxylase to increase HIF1α degradation[24]. Besides, the overexpression of PCBP2 can also inhibit the transcriptional activity of HIF1α to improve cellular lipid peroxidation (one of the major characteristics of ferroptosis)[35]. Under normoxic conditions, hydroxylation events suppress the accumulation of HIF1α, targeting it for degradation and inhibiting its binding to the lysophosphatidylcholine acyltransferase domain of CBP/p300. Conversely, under hypoxic conditions, the stabilization and transcriptional activity of HIF1α exhibit a switch-like dependence on oxygen concentration, showing a high−affinity interaction with CBP/p300[23]. Here, we found that HIF1α and CBP/p300 were synchronously increased, both in HIRI livers and HR- or erastin-stimulated hepatocytes, while decreased after PCBP2 being upregulated by ACT treatment (Fig. 6). However, the mechanism by which p300 catalyzes downstream target acetylation and subsequently modulates their functions to regulate the HIRI process remains elusive. Notably, our findings indicate that HMGB1 was upregulated and exhibited a negative correlation with PCBP2 in the liver under HIRI conditions. HIF1α was known to be upregulated early in HIRI and further induce the expression of HMGB1 through the anaerobic glycolysis pathway[36,37]. And notably, the nuclear export and secretion of HMGB1 were reported to be promoted *via* a CBP/p300-dependent mechanism that p300 and its homologue CBP could contribute to the lactate-induced lysine lactylation of nuclear HMGB1[21,22]. In this study, we observed that ACT concurrently attenuated the transcriptional activity of CBP/p300 and facilitated the nuclear retention of HMGB1, which might dependent upon the inhibition on lysine

lactylation of HMGB1 carried out by PCBP2 limiting HIF1α (Fig. 6). Furthermore, we confirmed that PCBP2 directly affected HMGB1 through HIF1α−p300 related signaling, which was verified by the enhanced acetylation of HMGB1 under CTB (p300 activator) stimulation and increased p300 under the HR insult.

As a member of the alarm DAMPs, HMGB1 is not only implicated in the initiation and progression of ferroptosis but also serves as a secreted phlogogenic product by ferroptotic cells[20,38,39]. Usually, the release of HMGB1 and the loss of cytoplasmic membrane integrity are regarded as the terminal of ferroptosis in cancers[40]. While in the non-cancer ferroptosis, HMGB1 also aggravated the injury of initiate ferroptosis cells due to the pro-inflammatory effects of HMGB1[38,41]. Recently, we demonstrated that hepatocyte-derived HMGB1 could exacerbate the deterioration of hepatic sinusoidal structure, aggravate the senility of LSECs and intensify the immune cell recruitment in HIRI[10]. Here, by employing immune cell analysis and flow cytometry on primary cells isolated from HIRI mice liver, we observed an augmentation of M1 macrophages in the livers affected by HIRI, potentially facilitated by the secretion of HMGB1 from hepatocytes into the surrounding microenvironment (Fig. 7). Importantly, the activation and recruitment of macrophages are the core of inducing extensive cell death and entering the inflammatory cytotoxic cycle in the HIRI liver[6]. Meantime, we discovered that ACT can inhibit the HIF1α−p300−HMGB1 signaling pathway by activating PCBP2, thereby reducing the recruitment of M1 macrophages and restoring the impaired hepatic immune microenvironment during HIRI. By specifically employing ApoE-LNPs to silence hepatocyte PCBP2, the protective effect of ACT on the PCBP2-oriented signaling network and the inhibition of M1 macrophage recruitment under HIRI were significantly reversed (Fig. 8). However, ACT was vulnerable to hydrolysis in the gastrointestinal tract, leading to degradation before absorption into the bloodstream, impacting its hepatoprotective properties[42,43]. Encouragingly, several delivery systems have been reported to improve the bioavailability of ACT[43]. Therefore, we may construct novel delivery systems for ACT to improve its bioavailability and extend clinical applications.

5. Conclusions

Our fundings substantiated that ACT alleviated hepatocyte ferroptosis under HIRI insult *via* promoting PCBP2 to maintain the stability of system Xc^- in balancing the iron transport and lipid peroxidation, and to inhibit the transcriptional activity of HIF1α/p300 for promoting HMGB1 nuclear export and M1 macrophage activation. This study revealed the significant potential of ACT as a novel therapeutic strategy for HIRI, offering a promising intervention approach for future integration into clinical practice.

Acknowledgments

This work was supported by the National Natural Science Foundation of China (Grant No. 82274186 to Xiaojiaoyang Li); National Key Research and Development Program on Modernization of Traditional Chinese Medicine (No. 2022YFC3502100 to Xiaojiaoyang Li, China); National High-Level Talents Special Support Program (China) to Xiaojiaoyang Li; Fundamental Research Funds for the Central Universities (Grant No. 2023-JYB-JBZD-046 to Xiaojiaoyang Li, China); High-level traditional Chinese medicine key subjects construction project of National Administration of Traditional Chinese Medicine-Beijing University of Chinese Medicine, Chinese Medicine Epidemic Disease (Grant No. zyyzdxk-2023264, China).

Author contributions

Kexin Jia: Writing − original draft, Methodology, Investigation, Data curation. Yinhao Zhang: Methodology, Data curation. Fanghong Li: Methodology. Runping Liu: Methodology. Jianzhi Wu: Methodology. Jiaorong Qu: Investigation. Ranyi Luo: Methodology. Zixi Huang: Methodology. Zhe Xu: Methodology. Xiaojiaoyang Li: Writing − review & editing, Supervision.

Conflicts of interest

The authors declare that there are no conflicts of interest.

Appendix A. Supporting information

Supporting information to this article can be found online at https://doi.org/10.1016/j.apsb.2025.03.002.

References

1. Hirao H, Nakamura K, Kupiec-Weglinski JW. Liver ischaemia-reperfusion injury: a new understanding of the role of innate immunity. *Nat Rev Gastroenterol Hepatol* 2022;**19**:239−56.
2. Schlegel A, Mergental H, Fondevila C, Porte RJ, Friend PJ, Dutkowski P. Machine perfusion of the liver and bioengineering. *J Hepatol* 2023;**78**:1181−98.
3. Xu B, Zhang P, Tang X, Wang S, Shen J, Zheng Y, et al. Metabolic rewiring of kynurenine pathway during hepatic ischemia−reperfusion injury exacerbates liver damage by impairing NAD homeostasis. *Adv Sci* 2022;**9**:e2204697.
4. Guan Y, Yao W, Yi K, Zheng C, Lv S, Tao Y, et al. Nanotheranostics for the management of hepatic ischemia−reperfusion injury. *Small* 2021;**17**:e2007727.
5. Fang X, Zhang J, Li Y, Song Y, Yu Y, Cai Z, et al. Malic enzyme 1 as a novel anti-ferroptotic regulator in hepatic ischemia/reperfusion injury. *Adv Sci* 2023;**10**:e2205436.
6. Du S, Zhang X, Jia Y, Peng P, Kong Q, Jiang S, et al. Hepatocyte HSPA12A inhibits macrophage chemotaxis and activation to attenuate liver ischemia/reperfusion injury *via* suppressing glycolysis-mediated HMGB1 lactylation and secretion of hepatocytes. *Theranostics* 2023;**13**:3856−71.
7. Protchenko O, Baratz E, Jadhav S, Li F, Shakoury-Elizeh M, Gavrilova O, et al. Iron chaperone poly rC binding protein 1 protects mouse liver from lipid peroxidation and steatosis. *Hepatology* 2021;**73**:1176−93.
8. Li J, Yuan J, Li Y, Wang J, Xie Q, Ma R, et al. D-Borneol enhances cisplatin sensitivity *via* autophagy dependent EMT signaling and NCOA4-mediated ferritinophagy. *Phytomedicine* 2022;**106**:154411.
9. Shen L, Zhang J, Zheng Z, Yang F, Liu S, Wu Y, et al. PHGDH inhibits ferroptosis and promotes malignant progression by upregulating SLC7A11 in bladder cancer. *Int J Biol Sci* 2022;**18**:5459−74.
10. Jia K, Zhang Y, Luo R, Liu R, Li Y, Wu J, et al. Acteoside ameliorates hepatic ischemia−reperfusion injury *via* reversing the senescent fate of liver sinusoidal endothelial cells and restoring compromised sinusoidal networks. *Int J Biol Sci* 2023;**19**:4967−88.
11. Mou JF, Lin XZ, Su HL, Lu HL, Liu QB, Liang B, et al. Anti-hepatitis B virus activity and hepatoprotective effect of des(rhamnosyl) verbascoside from *Lindernia ruellioides in vitro*. *Phytother Res* 2021;**35**:4555−66.
12. Cui Q, Pan Y, Zhang W, Zhang Y, Ren S, Wang D, et al. Metabolites of dietary acteoside: profiles, isolation, identification, and hepatoprotective capacities. *J Agric Food Chem* 2018;**66**:2660−8.

13. Zhang Y, Jia K, Li Y, Ma Z, Fan G, Luo R, et al. Radix Rehmanniae Praeparata aqueous extract improves hepatic ischemia/reperfusion injury by restoring intracellular iron homeostasis. *Chin J Nat Med* 2024;**22**:769−84.
14. Li M, Zhu M, Quan W, Huang W, Liu X, Zhang C, et al. Acteoside palliates D-galactose induced cognitive impairment by regulating intestinal homeostasis. *Food Chem* 2023;**421**:135978.
15. Lee KJ, Woo ER, Choi CY, Shin DW, Lee DG, You HJ, et al. Protective effect of acteoside on carbon tetrachloride-induced hepatotoxicity. *Life Sci* 2004;**74**:1051−64.
16. Ma D, Wang J, Liu L, Chen M, Wang Z. Acteoside as a potential therapeutic option for primary hepatocellular carcinoma: a preclinical study. *BMC Cancer* 2020;**20**:936.
17. Li X, Ge J, Li Y, Cai Y, Zheng Q, Huang N, et al. Integrative lipidomic and transcriptomic study unravels the therapeutic effects of saikosaponins A and D on non-alcoholic fatty liver disease. *Acta Pharm Sin B* 2021;**11**:3527−41.
18. Manoochehri H, Jalali A, Tanzadehpanah H, Taherkhani A, Najafi R. Aptamer-conjugated nanoliposomes containing *COL1A1* siRNA sensitize CRC cells to conventional chemotherapeutic drugs. *Colloids Surf B Biointerfaces* 2022;**218**:112714.
19. Chen Q, Zheng W, Guan J, Liu H, Dan Y, Zhu L, et al. SOCS2-enhanced ubiquitination of SLC7A11 promotes ferroptosis and radiosensitization in hepatocellular carcinoma. *Cell Death Differ* 2023;**30**:137−51.
20. Chen R, Kang R, Tang D. The mechanism of HMGB1 secretion and release. *Exp Mol Med* 2022;**54**:91−102.
21. Yang K, Fan M, Wang X, Xu J, Wang Y, Tu F, et al. Lactate promotes macrophage HMGB1 lactylation, acetylation, and exosomal release in polymicrobial sepsis. *Cell Death Differ* 2022;**29**:133−46.
22. Zheng S, Kummarapurugu AB, Afosah DK, Sankaranarayanan NV, Boothello RS, Desai UR, et al. 2-*O*, 3-*O* Desulfated heparin blocks high mobility group box 1 release by inhibition of p300 acetyltransferase activity. *Am J Respir Cell Mol Biol* 2017;**56**:90−8.
23. Berlow RB, Dyson HJ, Wright PE. Hypersensitive termination of the hypoxic response by a disordered protein switch. *Nature* 2017;**543**:447−51.
24. Nandal A, Ruiz JC, Subramanian P, Ghimire-Rijal S, Sinnamon RA, Stemmler TL, et al. Activation of the HIF prolyl hydroxylase by the iron chaperones PCBP1 and PCBP2. *Cell Metab* 2011;**14**:647−57.
25. Kim M, Jeong M, Hur S, Cho Y, Park J, Jung H, et al. Engineered ionizable lipid nanoparticles for targeted delivery of RNA therapeutics into different types of cells in the liver. *Sci Adv* 2021;**7**:eabf4398.
26. Chen MH, Liu XZ, Qu XW, Guo RB, Zhang L, Kong L, et al. ApoE-modified liposomes encapsulating resveratrol and salidroside alleviate manifestations of Alzheimer's disease in APP/PS-1 mice. *Drug Dev Ind Pharm* 2023;**49**:559−71.
27. Zhou X, You F, Chen H, Jiang Z. Poly(C)-binding protein 1 (PCBP1) mediates housekeeping degradation of mitochondrial antiviral signaling (MAVS). *Cell Res* 2012;**22**:717−27.
28. Frey AG, Nandal A, Park JH, Smith PM, Yabe T, Ryu MS, et al. Iron chaperones PCBP1 and PCBP2 mediate the metallation of the dinuclear iron enzyme deoxyhypusine hydroxylase. *Proc Nat Acad Sci U S A* 2014;**111**:8031−6.
29. Bae DH, Lane DJR, Siafakas AR, Sutak R, Paluncic J, Huang MLH, et al. Acireductone dioxygenase 1 (ADI1) is regulated by cellular iron by a mechanism involving the iron chaperone, PCBP1, with PCBP2 acting as a potential co-chaperone. *Biochim Biophys Acta, Mol Basis Dis* 2020;**1866**:165844.
30. Braconi C, Valeri N, Kogure T, Gasparini P, Huang N, Nuovo GJ, et al. Expression and functional role of a transcribed noncoding RNA with an ultraconserved element in hepatocellular carcinoma. *Proc Nat Acad Sci U S A* 2011;**108**:786−91.
31. Guo S, Chen Y, Yang Y, Zhang X, Ma L, Xue X, et al. TRIB2 modulates proteasome function to reduce ubiquitin stability and protect liver cancer cells against oxidative stress. *Cell Death Dis* 2021;**12**:42.
32. Xiang L, Zeng Q, Liu J, Xiao M, He D, Zhang Q, et al. MAFG-AS1/MAFG positive feedback loop contributes to cisplatin resistance in bladder urothelial carcinoma through antagonistic ferroptosis. *Sci Bull* 2021;**66**:1773−88.
33. Yang WS, Stockwell BR. Ferroptosis: death by lipid peroxidation. *Trends Cell Biol* 2016;**26**:165−76.
34. Chen X, Yu C, Kang R, Kroemer G, Tang D. Cellular degradation systems in ferroptosis. *Cell Death Differ* 2021;**28**:1135−48.
35. Xia N, Tang Z, Wang C, Xu G, Nie X, Zhang W, et al. PCBP2 regulates hepatic insulin sensitivity *via* HIF-1α and STAT3 pathway in HepG2 cells. *Biochem Biophys Res Commun* 2015;**463**:116−22.
36. Kang R, Zeng L, Xie Y, Yan Z, Zhou B, Cao L, et al. A novel PINK1- and PARK2-dependent protective neuroimmune pathway in lethal sepsis. *Autophagy* 2016;**12**:2374−85.
37. Jiang J, Wang GZ, Wang Y, Huang HZ, Li WT, Qu XD. Hypoxia-induced HMGB1 expression of HCC promotes tumor invasiveness and metastasis *via* regulating macrophage-derived IL-6. *Exp Cell Res* 2018;**367**:81−8.
38. Davaanyam D, Lee H, Seol SI, Oh SA, Kim SW, Lee JK. HMGB1 induces hepcidin upregulation in astrocytes and causes an acute iron surge and subsequent ferroptosis in the postischemic brain. *Exp Mol Med* 2023;**55**:2402−16.
39. Efimova I, Catanzaro E, Van der Meeren L, Turubanova VD, Hammad H, Mishchenko TA, et al. Vaccination with early ferroptotic cancer cells induces efficient antitumor immunity. *J Immunother Cancer* 2020;**8**:e001369.
40. Wiernicki B, Maschalidi S, Pinney J, Adjemian S, Vanden Berghe T, Ravichandran KS, et al. Cancer cells dying from ferroptosis impede dendritic cell-mediated anti-tumor immunity. *Nat Commun* 2022;**13**:3676.
41. Vats K, Kruglov O, Mizes A, Samovich SN, Amoscato AA, Tyurin VA, et al. Keratinocyte death by ferroptosis initiates skin inflammation after UVB exposure. *Redox Biol* 2021;**47**:102143.
42. Wu YT, Lin LC, Sung JS, Tsai TH. Determination of acteoside in *Cistanche deserticola* and *Boschniakia rossica* and its pharmacokinetics in freely-moving rats using LC−MS/MS. *J Chromatogr B Analyt Technol Biomed Life Sci* 2006;**844**:89−95.
43. Xiao Y, Ren Q, Wu L. The pharmacokinetic property and pharmacological activity of acteoside: a review. *Biomed Pharmacother* 2022;**153**:113296.